J. Fluid Mech. (2000), *vol.* 424, *pp.* 127–167. Printed in the United Kingdom

Passive scalar dispersion in a turbulent boundary layer from a line source at the wall and downstream of an obstacle

By J.-Y. VINÇONT, S. SIMOËNS, M. AYRAULT AND J. M. WALLACE†

Laboratoire de Mécanique des Fluides et d'Acoustique, UMR CNRS 5509, Ecole Centrale de Lyon, BP 163-69131 Ecully, France

(Received 19 October 1998 and in revised form 28 June 2000)

Simultaneous measurements of the velocity and scalar concentration fields have been made in the plume emitting from a two-dimensional line source at the wall. The source is one obstacle height, h, downstream of a two-dimensional square obstacle located on the wall of a turbulent boundary layer. These measurements were made in two fluid media: water and air. In both media particle image velocimetry (PIV) was used for the velocity field measurements. For the scalar concentration measurements laser-induced fluorescence (LIF) was used for the water flow and Mie scattering diffusion (MSD) for the air flow. Profiles of the mean and root-mean-square streamwise and wall-normal velocity components, Reynolds shear stress and mean and root-mean-square scalar concentration were determined at $x = 4h$ and $6h$ downstream of the obstacle in the recirculation region and above it in the mixing region. At these streamwise stations the scalar fluxes, $\overline{uc}$ and $\overline{vc}$, were also determined from the simultaneous velocity and scalar concentration field data. Both of these fluxes change sign from negative to positive with increasing distance from the wall in the recirculating region at $4h$.

A conditional analysis of the data was carried out by sorting them into the eight categories (octants) given by the sign combinations of the three variables: $\pm u$, $\pm v$ and $\pm c$. The octants with combinations of these three variables that correspond to types of scalar concentration flux motions that can be approximated by mean gradient scalar transport models are the octants that make the dominant contributions to $\overline{uc}$ and $\overline{vc}$. However, in the recirculating zone, counter-gradient transport type motions also make significant contributions. Based on this conditional analysis, second-order mean gradient models of the scalar and the momentum fluxes were constructed; they compare well to the measured values at $4h$ and $6h$, particularly for the streamwise scalar flux, $\overline{uc}$.

Additional measurements of the velocity and concentration fields were made further downstream of the reattachment location in the wake region of the air flow. The mean velocity deficit profile determined from these measurements at $x = 20h$ compares quite well to a similarity solution profile obtained by Counihan, Hunt & Jackson (1974). Their analysis was extended in the present investigation to the concentration field. The similarity solution obtained for the mean concentration compares well to profiles measured at $x = 12h$, $15h$, and $20h$, up to about three obstacle heights above the wall.

---

† Permanent address: Department of Mechanical Engineering, University of Maryland, College Park, MD 20742, USA.

1. Introduction

In large cities all over the world the number of automobiles and other pollution sources is steadily growing. One of the most obvious consequences of this growth has been the deterioration of air quality in the urban canopy where human habitation is concentrated. Recently, some cities have deployed permanent sensors to obtain instantaneous information about the air quality state. However, it is much more difficult to *predict* peaks in pollution and their evolution. Knowledge of the levels of pollutants in cities is of interest at a wide range of scales: from the very large, at the scale of the atmosphere, to the quite small, at the scale of a few streets or buildings. At the small scales of interest, dispersion from ground level sources in the proximity of one or more obstacles in the neighbourhood is quite common. Experiments to measure flow properties related to turbulent scalar transport are necessary for a better understanding of the physical processes involved in dispersion and mixing from such pollutant sources. Although laboratory flows such as the ones described in this paper have orders of magnitude lower Reynolds numbers than urban canopy atmospheric flows, experimental data from them provide the controlled conditions necessary for testing prediction methods and models. They also give some insight into the underlying scalar transport processes.

The equation describing the evolution of instantaneous scalar concentration, $C(x, y, z, t)$, in a flow region with velocity components U_i is

$$\frac{\partial C}{\partial t} + U_i \frac{\partial C}{\partial x_i} = \mathscr{D} \frac{\partial^2 C}{\partial x_i^2} + Q, \tag{1.1}$$

where $\mathscr{D}$ is the molecular diffusion coefficient of the scalar species, the Cartesian coordinate directions x_i ($i = 1 - 3$) are x, y and z with U, V and W velocity components in these directions and the source strength is Q, with units of scalar mass per unit source slot span per unit time for the source considered herein. With Reynolds decomposition and averaging of equation (1.1), the evolution equation for the mean scalar concentration is

$$\frac{\partial \overline{C}^*}{\partial t^*} + \overline{U}_i^* \frac{\partial \overline{C}^*}{\partial x_i^*} = \frac{1}{Sc\ Re_h} \frac{\partial}{\partial x_i^*} \left(\frac{\partial}{\partial x_i^*} \overline{C}^* - \overline{u_i c}^* \right) + \overline{Q}^*, \tag{1.2}$$

where overbars represent mean values, lower-case variables are fluctuations about the mean values, and the superscript * indicates normalized variables. For the case of the two experiments described below, the normalizing scales are the free-stream velocity, U_e, the obstacle height, h, and the mean scalar concentration at the source slots, $\overline{C}_s$. The Reynolds number, $Re_h \equiv U_e h/\nu$, the Schmidt number, $Sc \equiv \nu/\mathscr{D}$ and the non-dimensional source strength, $\overline{Q}^* \equiv (V_s \overline{C}_s d_s)/(U_e \overline{C}_s h)$, where the subscript s denotes values at the slots, V_s is the wall normal velocity there and d_s is the slot opening size in the x-direction. Thus the normalized variables, $\overline{C}^*$ and $\overline{U}_i^*$, are functions of the normalized flow location, x_i^*, but also of the flow parameters, Re_h, Sc and $\overline{Q}^*$. All the terms of equation (1.2) in principle can be measured (see Britter 1989). However, the scalar flux terms, $\overline{u_i c}^*$, are very difficult to obtain, and few results have been published.

In the last twenty-five years a few different techniques have been developed to measure these scalar fluxes. Antonia, Prahu & Stephenson (1975) and Browne & Antonia (1986) combined hot-and cold-wire anemometry to measure heat fluxes in a turbulent jet and wake respectively, where temperature was considered as a passive scalar. Quite recently Wallace *et al.* (1995) combined hot-wire anemometry with high-speed movie filming of Mie scattering diffusion (MSD) from smoke particles to

measure the $\overline{u_i c}$ fluxes in the plume downstream of a line source on the wall of a turbulent boundary layer. In addition to the long time required to make measurements at a sufficient number of locations, a more restrictive drawback of such combined techniques employing hot wires is the impossibility of their use in complex flow situations, such as in recirculating flow zones.

Optical techniques avoid this limitation. One of the first examples is the investigation of Gad-el-Hak & Morton (1979) involving the dispersion of smoke in a turbulent air jet with a coflowing turbulent air stream. They combined a light scattering technique with laser Doppler anemometry (LDA) to simultaneously measure the velocity components and the instantaneous mass fraction of the smoke. More recently Papanicolaou & List (1988), Papantoniou & List (1989) and Lemoine, Wolff & Lebouche (1996) developed optical methods coupling LDA and LIF. Papanicolaou & List and Papantoniou & List applied these combined techniques to a fluorescent dye plume in a buoyant water jet, while Lemoine *et al.* investigated a submerged turbulent water jet. However, like the hot-wire methods, these were also still single-point measurements, making it quite difficult to study a large field or non-stationary conditions.

In order to make planar scalar flux measurements in complex flow conditions, Simoëns, Ayrault and coworkers (Simoëns 1992; Simoëns & Ayrault 1994; Ayrault & Simoëns 1995; Simoëns *et al.* 1996) have developed a technique combining particle image velocimetry (PIV) and laser-induced fluorescence (LIF) for water flow that was later extended to PIV and MSD for air flow. Data were acquired simultaneously in a substantial portion of the illuminated plane rather than at single locations. Properties of the concentration and velocity fields obtained in these investigations were compared to results available in the literature to validate these two combinations of methods. These measurement methods are the ones used in the present investigation.

Although a number of investigations have focused on properties of the concentration fields of scalar releases from point and line sources in or at the walls of turbulent boundary layers (see Poreh & Cermak 1964; Fackrell & Robins 1982; Sawford, Frost & Allan 1985; Dinar, Kaplan & Kleinmann 1988 and Gong 1991), only the study of Fackrell & Robins includes scalar flux measurements. Some of these investigations include hills or other obstacles, and a relatively recent study by Trombetti & Tampieri (1992) even considered scalar dispersion from elevated sources in a flow past two-dimensional obstacles. However, none of these previous investigations had conditions closely similar to those in the present experiment. The objective of our investigation was to *simultaneously* measure the velocity and concentration fields in the neighbourhood of and in the recirculation and wake regions downstream of a two-dimensional obstacle located on the wall of a turbulent boundary layer. This obstacle was located just upstream of a two-dimensional line source emitting a passive scalar plume at the wall. These measurements are intended to provide physical insight into the scalar transport processes that will aid in constructing and testing predictive models of this and similar flows.

In § 2 the experiments carried out in the water channel and wind tunnel are described. Preliminary measurements of some velocity field statistical properties obtained with the PIV system in both water and air are presented for smooth-wall turbulent boundary layers with no obstacles on the wall. These measurements demonstrate the acceptability of using the PIV system for the more complex flow with an obstacle on the wall. The results of the velocity, concentration and concentration flux measurements downstream of the obstacle are presented and discussed in § 3. This includes a conditional analysis of the data in § 3.4 for the recirculation region that

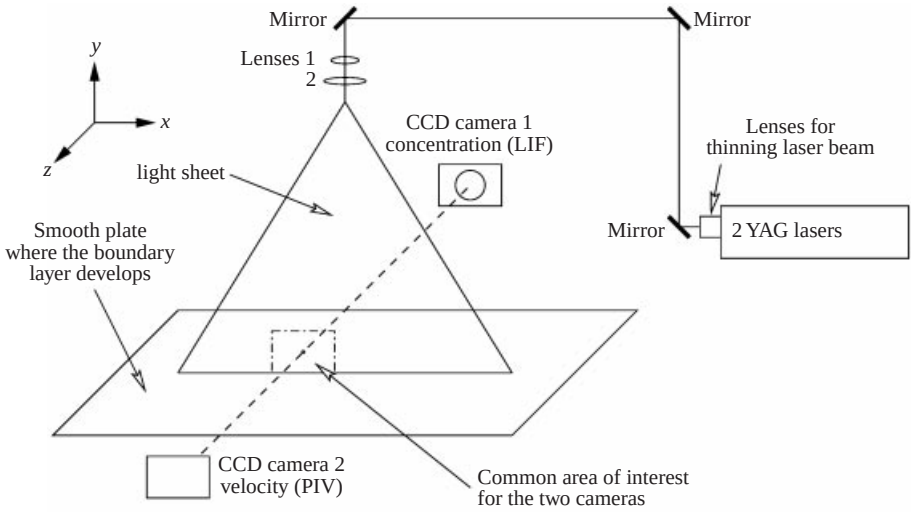

FIGURE 1. Optical arrangement to create laser light sheets.

gives some further insight into the physics of the scalar transport in this complex flow. Using insights gained from this conditional analysis, in § 3.5 we construct simple models of the scalar fluxes, $\overline{uc}$ and $\overline{vc}$, and the momentum flux, $\overline{uv}$, and compare their computed values to the measurements. In § 3.6 we compare computed values of the mean velocity deficit using the similarity analysis of Counihan, Hunt & Jackson (1974) to values measured in the wake region. We also extend their similarity analysis to the concentration field and compare values of the mean concentration computed from the analysis to the measured values. Conclusions are drawn in § 4. Additional details about the experiments and their analysis are given in Vinçont (1999).

2. Description of experiments

The methods developed by Simoëns (1992), Simoëns & Ayrault (1994), Ayrault & Simoëns (1995) and Simoëns *et al.* (1996) were applied in the present case to a more complex flow. As mentioned above, this is the flow downstream of a two-dimensional square obstacle of cross-section h^2 located on the wall of a turbulent boundary layer and oriented perpendicular to the mean flow direction. A line source at the wall emitted a passive scalar on the lee side, a distance of one obstacle height downstream. Two experiments were carried out. The first was in an open water channel with PIV and LIF; the second was in a wind tunnel using PIV and MSD. As in the previous work of Simoëns, Ayrault and coworkers, two synchronized YAG lasers for flow illumination and two CCD cameras facing each other for image capture were used. The optical arrangement for both experiments is shown schematically in figure 1. The YAG lasers provide 300 mJ of energy per pulse and have a recharging frequency of 10 Hz. This recharging frequency precludes temporally resolving the evolution of the flow field. However, statistical information about the velocity, the concentration and the concentration flux fields can be obtained much more readily than with single-point measurement methods that employ hot-wire or laser Doppler anemometry.

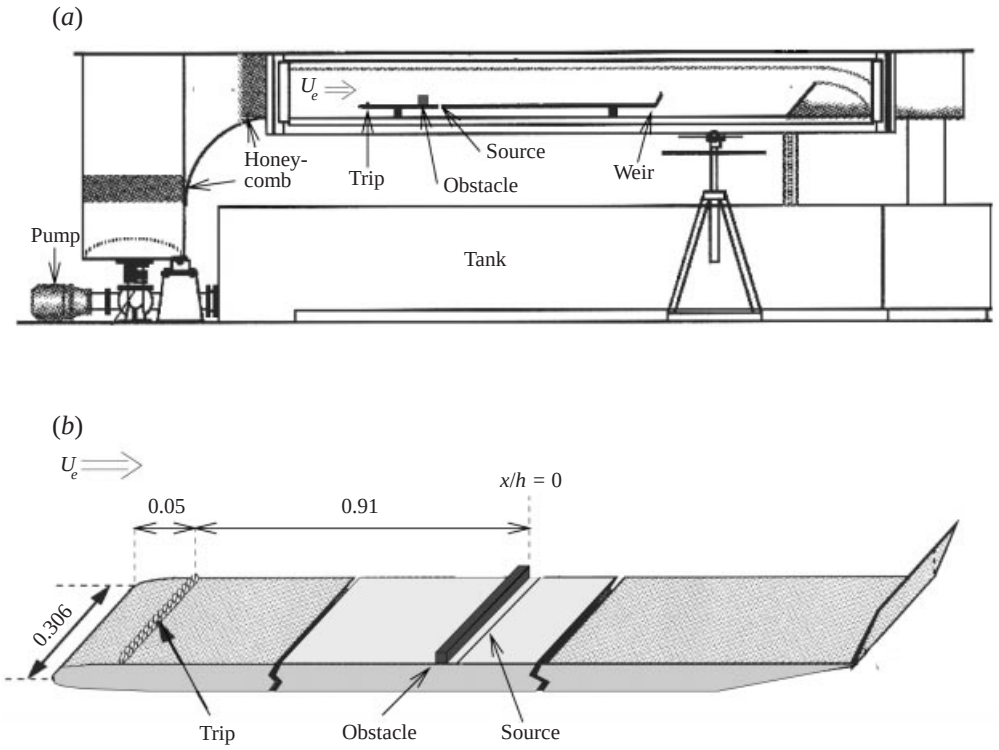

FIGURE 2. Sketch of water channel. Dimensions in metres.

2.1. *Water flow experiment*

The water flow boundary layer developed on a flat plate with a rounded leading edge that is elevated above the floor of the 30.6 cm wide and 2.56 m long open channel flume sketched in figure 2. The free surface is 17 cm above the flat plate. The free-stream velocity of the flow above the boundary layer, U_e, was maintained at 10 cm s^{-1}, a speed at which free-surface disturbances were minimal. A 8 mm high sawtooth trip initiated the boundary layer about 5 cm from the leading edge of the flat plate. An $h^2 = 7\,\text{mm} \times 7\,\text{mm}$ cross-section square rod with an aspect ratio of about 44 was placed spanwise across the flat plate, from sidewall to sidewall of the channel, 91 cm downstream of the trip. At this x-location, the thickness of the boundary layer δ, without the obstacle in place was about 5 cm, so that the ratio, $\delta/h \approx 7$. This ratio is the principal parameter that determines the extent of the recirculating zone behind the obstacle where there is a large separation region with reverse flow directed upstream near the wall. With δ/h of 7, previous investigations, such as that of Schofield & Logan (1990), have indicated that the recirculation zone extends about $7h$ downstream of the obstacle, close to the value of about $6.5h$ that we found in this investigation. The Reynolds number of the boundary layer, $R_\theta \equiv U_e\theta/\nu$, was 560, where $\theta = 5.3$ mm is the momentum thickness without the obstacle, but at its x-location, and ν is the kinematic viscosity. The Reynolds number based on the obstacle height and the free-stream velocity, Re_h, was approximately 700. The friction velocity $u_\tau = 0.0051\,\text{m s}^{-1}$, for the conditions without the obstacle, was determined iteratively by the Clauser method, and was used to scale the preliminary velocity data obtained without the obstacle in place.

The water channel flow was seeded throughout with Iriodine 110 solid particles of approximately 15 μm diameter and 3 g cm^{-3} density. Particles of this type follow the flow quite faithfully making them suitable for the PIV measurements. An estimate of the mean particle response time to a step change in velocity is about 2×10^{-5} s, while the highest turbulent frequency in this flow, as determined from velocity spectra, has a period of about 2×10^{-2} s. These particles were successively illuminated by a pair of light sheets in the (x, y)-plane along the centreline of the flat plate. These light sheets were generated by passing the YAG laser beams through two cylindrical lenses in series, as illustrated in figure 1, to obtain light sheet thicknesses of less than 0.5 mm.

The CCD camera used for PIV was fitted with a Cokin No. A004 filter that transmitted the reflected light from the Iriodine particles and removed most of that from the dispersed fluorescent dye that seeped into the flow at the wall, as will be described in more detail below. The small time interval, Δt, separating the pair of light sheets could be varied depending on the mean speed of the flow in the region in which the PIV images were obtained. For this water flow experiment a single value of $\Delta t = 7.23$ ms was selected, but it was varied for the air flow experiment. The PIV CCD camera was synchronized with the pulse rate of the pair of lasers by means of a timing signal. The CCD camera then transmitted an analog signal carrying the successive particle image pairs at the standard video rate of 50 Hz so that they were recorded on successive video frames. Because the framing rate of the video recorder is 50 Hz and the pulse rate of the lasers was 10 Hz, between the recorded pairs of images on successive frames eight frames were left blank and were unused. All the pairs of images were recorded however.

For this water channel experiment, the concentration field CCD camera had a large field of view: about 85 mm × 55 mm, in the x- and y-directions, respectively. The PIV CCD camera was zoomed into a smaller subfield of this concentration field of view, approximately 17 mm × 11 mm, corresponding to about $2.4h$ in the x- and $1.6h$ in the y-directions. Because the PIV field of view was smaller than that of the concentration field, the PIV CCD camera had to be moved vertically at each x-location to image several different overlapping regions in order to obtain complete vertical velocity and concentration flux profiles. The images from the two cameras were recorded on video tapes with two video recorders. The synchronization of the pair of video recordings was made by interrupting the laser light sheets momentarily and using the end of this interruption as the first synchronized pair.

An instantaneous realization of the concentration CCD camera field of view is shown in the example video frame of figure 3(a) where the obstacle is on the left, and the highly concentrated fluorescent dye is above and primarily downstream of the wall source. The subfield obtained with the zoomed PIV CCD camera also is indicated in (a). A portion of the image above the plume and below the wall has been removed because these regions contain no useful information. As is customary, this PIV subfield of view is further divided into a mesh of small subzones with dimensions of about $0.3h$ in the x- and $0.2h$ in the y-directions. In these subzones the local instantaneous U and V velocity components in the illuminated plane are determined by digitally cross-correlating the images of the Iriodine particles in each subzone at successive times, as will be discussed in more detail in the Appendix. The successive images of these particles, corresponding to the PIV subfield and separated in time by Δt, are shown in part (b) of figure 3. The correlation map showing the correlation peak (white dots) in each of the 49 subzones of the PIV field of view is shown in part (c); the distance from the centre of each subzone to the cross-correlation peak is the average distance the particles in the subzone have been displaced in

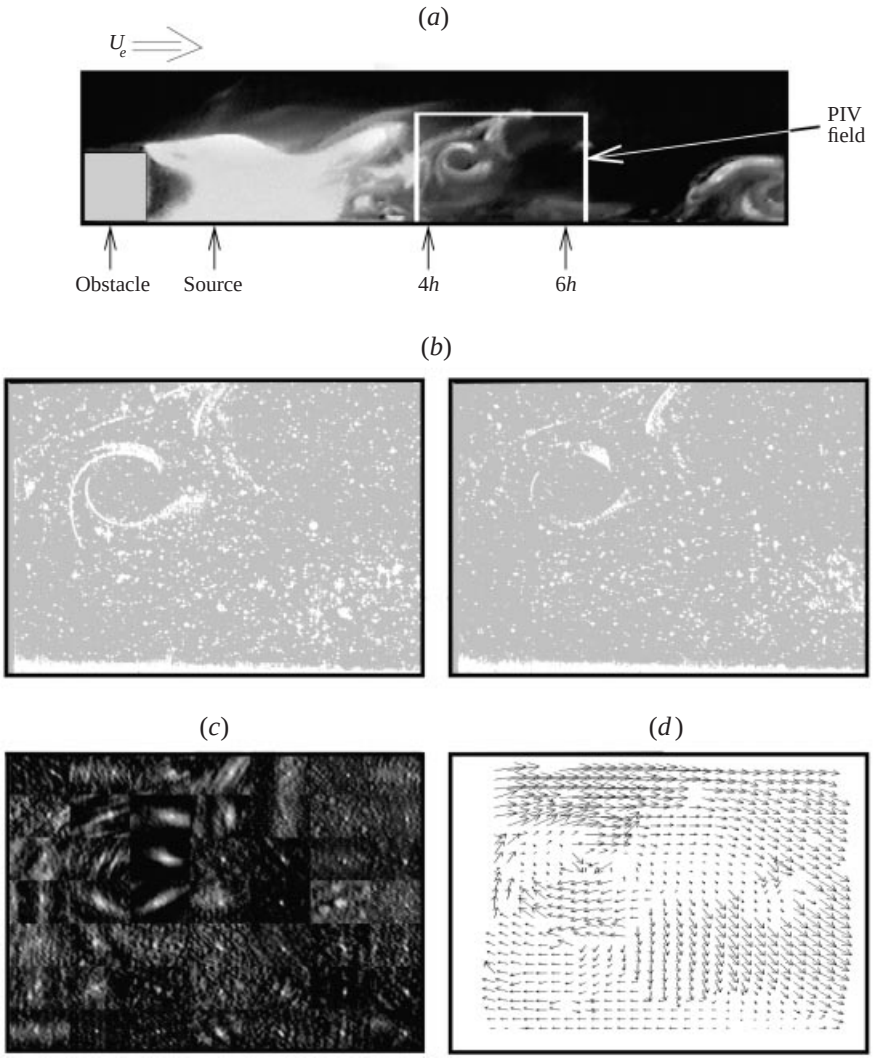

FIGURE 3. (*a*) Instantaneous video image of scalar plume released from line source slot, 1*h* downstream of square obstacle of cross-section h^2 located on the wall of the water channel. Scalar is Rhodamine B fluorescent dye. Iriodine particles are also seeded into flow and are imaged in zoomed PIV subfield marked by the box in the figure. (*b*) Pair of PIV subfield images of Iriodine particles with Δt time separation. All such pairs are cross-correlated to determine the velocity components in the plane. (*c*) Correlation map. (*d*) Projection of velocity vector field on the image plane.

the time interval Δt. Knowing these distances permits the calculation of the velocity components, U and V, in the horizontal and vertical directions, x and y, of this plane. Additional velocity component vectors can be obtained by displacing the locations of the cross-correlation subzones in both the x- and y-directions by small incremental distances so that the subzones overlap. The velocity component vector field resulting from this process for this example pair of images is shown in part (*d*) of the figure. The cross-correlation map in (*c*) shows the subzones without overlap, but the velocity vector field in (*d*) incorporates this overlapping procedure.

A 1 mm wide rectangular slot, parallel to the obstacle, located 1*h* downstream of it and spanning the floor of the channel, was the two-dimensional source for the scalar

plume. The passive scalar that seeped into the water boundary layer through this slot was Rhodamine B, a fluorescent dye with a maximum emission wavelength of 575 nm and a Schmidt number, Sc, of about 2500. A solution of the dye and water, seeded with the Iriodine particles, was delivered by a simple gravitation system to the slot at a small and very constant flow rate after it was mixed by passing it through two screens stretched across a box mounted below the slot. The speed of the dye and water solution, seeded with particles and exiting the slot, was estimated to be about $0.4\,\mathrm{cm\,s^{-1}}$, i.e. less than 5% of U_e, and the normalized source strength $\overline{Q}^* \approx 5.7 \times 10^{-3}$, with units of $\overline{Q}$ as $\mathrm{g\,s^{-1}m^{-1}}$. The source concentration, C_s, was measured just above the slot for both the water and air flow experiments. The CCD camera used to record the light intensity was fitted with a Dichroic filter with a 10 nm bandwidth centred on the 575 nm wavelength of the dye. The reflected light from the Iriodine 110 particles, with the 532 nm wavelength of the YAG lasers, was thereby removed, and the light recorded was only that emitted by the fluorescent dye and any residual background light. Before the images were recorded with the Iriodine particles and the Rhodamine B dye in the flow, a sequence of background light sheet intensity images was recorded. These background light intensity images were subsequently averaged and subtracted from the digitized images of the fluorescent dye in post-processing, as described in the Appendix.

The dynamic range of the CCD camera was not great enough simultaneously to record, without saturating, the low levels of light intensity in the flow region well downstream of the obstacle and, with the same aperture, the very high levels in the region close to the source. Therefore, after looking at the signal level on an oscilloscope to obtain the maximum dynamic range without saturating for each downstream location where the concentration and concentration fluxes were to be measured, an aperture opening of $f^{\#} = 1.4$ was chosen. Then the camera aperture was reduced to $f^{\#} = 5.6$, and the concentration field was re-recorded in order to obtain the light intensity at the source without saturation. In figure 3(a) the image is saturated in the very bright white region above the source and just upstream of the $4h$ location above the level of the top of the obstacle. This is because the aperture of $f^{\#} = 1.4$ was used to measure the concentration with maximum dynamic range in the region of the plume where the PIV data were taken.

The physical principal on which the measurement of scalar concentration with LIF is based is the capacity of fluorescent dye to absorb incident light at one wavelength and to re-emit light at a different wavelength. The re-emitted light is proportional to the concentration of the fluorescent dye at the point of measurement. This proportionality is expressed by the Beer–Lambert law and can be shown to be linear under certain conditions. The application of LIF to quantitatively measure scalar concentration has been developed in numerous investigations (e.g. see Simoëns & Ayrault 1994).

The principal difficulty with the use of LIF is the absorption of light all along the effected path: between the CCD camera and the point of measurement, L_f, and between this point and the source of the incident light ray, L_i. Nearly linear proportionality between the intensity of the light recorded and the concentration can be obtained by using a weak concentration of dye and by minimizing the total optical path. The intensity of the light, I, that arrives at a cell of the CCD camera resulting from an instantaneous concentration of the scalar at the point of measurement, $C(x, y, z, t)$, can be expressed as

$$I = A \times C(x, y, z, t) \times F(absorption). \tag{2.1}$$

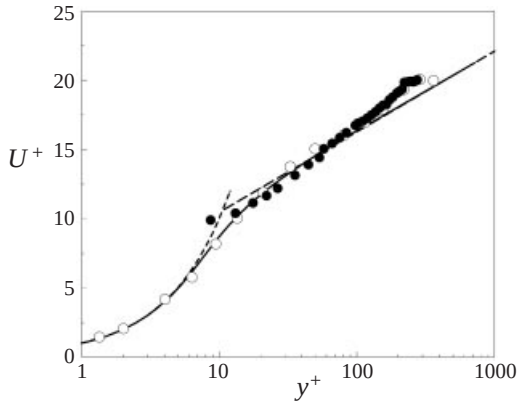

FIGURE 4. Mean velocity profile in the water channel: open circles, F. Laadhari (personal communication) with LDA, $R_\theta = 570$; filled circles, present PIV data, $R_\theta = 560$; short dashes $U^+ = y^+$; long dashes $U^+ = 2.5 \ln y^+ + 5.5$; solid line, fit of data from literature by Spalding (1961).

A is an absorption coefficient that is independent of spatial location in the flow and of time. The function $F(absorption)$ depends on both the measurement point and time, (x, y, z, t), and is developed in detail by Simoëns & Ayrault (1994). We note here that F is a function of L_i, L_f, ε_i and ε_f. The last two parameters are the respective absorption coefficients for the two parts of the optical path. For the present investigation $L_{i_{max}} = 17\,\text{cm}$, $L_{f_{max}} = 15\,\text{cm}$, $\varepsilon_i = 21\ \ell\,\text{g}^{-1}\,\text{cm}$, $\varepsilon_f = 93\ \ell^{-1}$ and $C_{s_{max}} = 5 \times 10^{-4}\ \text{g}\ \ell^{-1}$, where $C_{s_{max}}$ is the maximum concentration at the source of the fluorescent dye. With these values of these parameters

$$F \approx \mathrm{e}^{-(\varepsilon_i C_{s_{max}} L_{i_{max}})} e^{-(\varepsilon_f C_{s_{max}} L_{f_{max}})} \tag{2.2}$$

is approximately unity. Therefore, for the present case, the conditions are fulfilled to have a nearly linear proportionality between the concentration of the scalar at the measurement point and the light intensity received by a cell of the CCD camera.

2.1.1. *Preliminary PIV measurements in boundary layer without an obstacle*

To confirm that this water channel flow showed standard zero-pressure-gradient flat-plate boundary layer properties and that the PIV system could measure these properties with sufficient accuracy, a preliminary PIV set of images was recorded and processed as described above and in the Appendix. They are compared here to LDA results of F. Laadhari (1998, personal communication) obtained earlier in the same channel at $R_\theta = 570$, i.e. for almost identical conditions, and to direct numerical simulation (DNS) boundary layer results of Spalart (1988) at $R_\theta = 670$ and 1410. The mean velocity profiles are shown in figure 4 along with the logarithmic relation, $U^+ = 2.5 \ln y^+ + 5.5$, the linear relationship, $U^+ = y^+$, and the curve fit of Spalding (1961). The normalized mean velocity is plotted as $U^+ \equiv \overline{U}/u_\tau$ against $y^+ \equiv y u_\tau / \nu$, where the overbar denotes time-averaged values, u_τ is the friction velocity and y is the distance from and normal to the wall. Although the PIV data show small discontinuities at the y^+ locations where the CCD camera was displaced, the general agreement with the LDA data is very good, except for the PIV value in the lower part of the buffer layer and closest to the wall. At this position the PIV assumption of a negligible instantaneous velocity gradient across the measurement area is not very well fulfilled. However, the mean shear in the flow downstream of the obstacle where

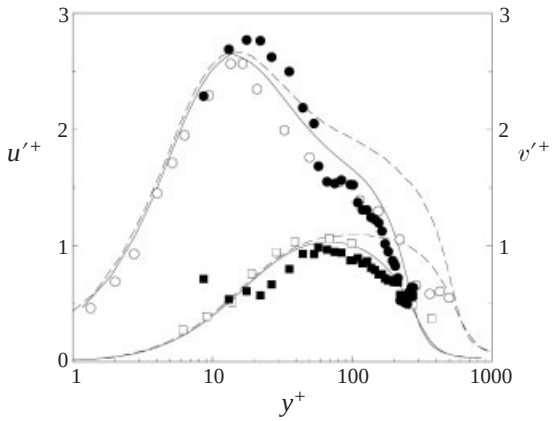

FIGURE 5. Root-mean-square velocity fluctuation profiles in the water channel: circles, u'^+; squares, v'^+. Open symbols, F. Laadhari (personal communication) with LDA, $R_\theta = 570$; filled symbols, present PIV data, $R_\theta = 560$; solid lines, Spalart's (1988) DNS, $R_\theta = 670$ and dashed lines, $R_\theta = 1410$.

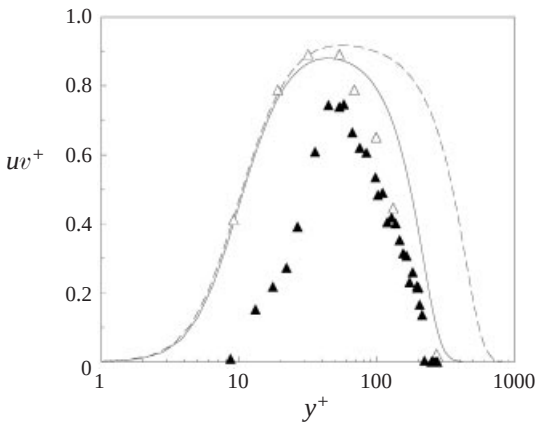

FIGURE 6. Reynolds shear stress profile, uv^+, in the water channel: open triangles, F. Laadhari (personal communication) with LDA, $R_\theta = 570$; filled triangles, present PIV data, $R_\theta = 560$; solid line, Spalart's (1988) DNS, $R_\theta = 670$ and dashed line, $R_\theta = 1410$.

the definitive measurements were made is everywhere less than that at $y^+ \approx 20$ of this obstacle-free boundary layer.

The profiles of the root-mean-square (r.m.s.) streamwise and wall-normal velocity component fluctuations, u'^+ and v'^+, are shown in figure 5, where the superscripts $'$ and $^+$ denote r.m.s. values normalized by the friction velocity. The agreement between the PIV and LDA results is fairly good, although the PIV values of u'^+ are a little larger than the LDA measurements in the buffer and lower logarithmic regions, and the PIV values of v'^+ are a little smaller. For the y^+ position closest to the wall the v'^+ value is clearly much too large.

When the streamwise and wall-normal fluctuations are correlated, the Reynolds shear stress is obtained. This profile, normalized by u_τ^2, is shown in figure 6. For positions greater than $y^+ \approx 60$ the agreement with the LDA values is reasonably good. By contrast, nearer the wall where the local shear is large, these preliminary PIV test data lie considerably below the LDA and simulated comparison values. The

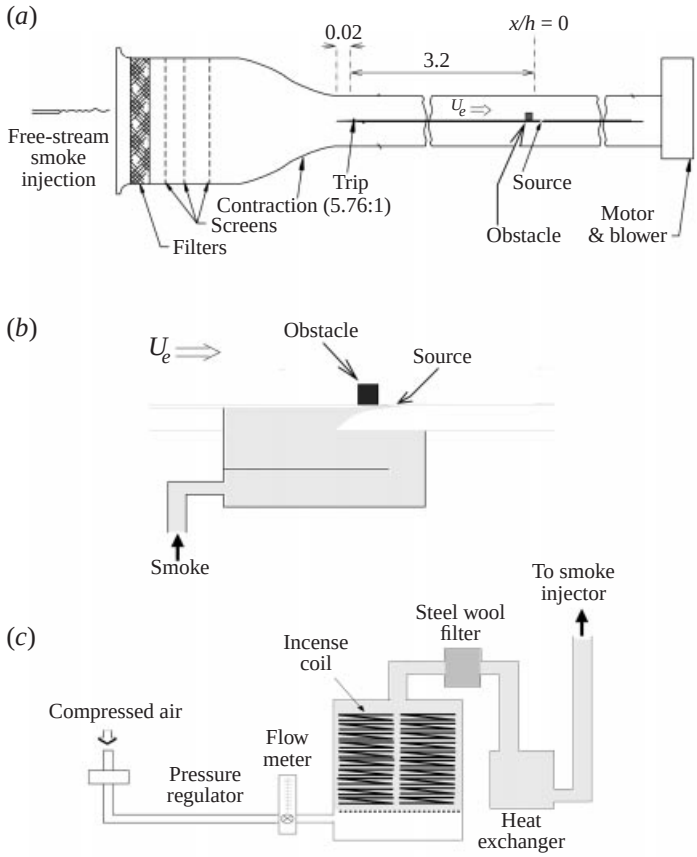

FIGURE 7. Sketch of the wind tunnel. Dimensions in metres.

Reynolds stress measurements appear to be particularly sensitive to the presence of high shear in the PIV image field.

2.2. *Wind tunnel experiment*

The air boundary layer developed on a flat plate mounted at the horizontal mid-plane of the 0.5 m × 0.5 m test section of the wind tunnel, is sketched in figure 7. The flat plate has a sharp leading edge. Sand paper and a 5 mm diameter round rod, placed about 2 cm downstream of the leading edge, were used to initialize and stabilize the laminar-turbulent transition of the boundary layer. As for the water channel experiment, a narrow slot in the flat plate, extending across its full span, was the source of the scalar plume. The slot was installed 3.2 m downstream of the flat-plate leading edge in order to allow a sufficiently thick turbulent boundary layer to develop. For the $U_e = 2.3\,\mathrm{m\,s^{-1}}$ speed of the free-stream flow that was maintained for the experiment, the boundary layer thickness, δ, at this x-location was about 7 cm, and R_θ was approximately 980, with $\theta \approx 6.3$ mm and the friction velocity, $u_\tau \approx 0.106\,\mathrm{m\,s^{-1}}$. To maintain geometric similarity with the water channel experiment, for the wind tunnel experiment the square rod obstacle had a cross-section of 1 cm × 1 cm, thus maintaining the 1/7 ratio of the obstacle height to the boundary layer thickness. This obstacle also spanned the channel and had an aspect ratio of 50. As in the water channel experiment, it was located a distance of $1h$ upstream of and parallel to the

scalar source slot. The Reynolds number, Re_h, based on the obstacle height and the free-stream velocity was approximately 1500.

For this air flow experiment, the passive scalar that seeped into the flow through the source slot was dry incense smoke with a particle diameter range of approximately 0.1–3.0 μm, a mean particle diameter of about 0.9 μm and a standard deviation of about 0.5 μm (K.-F. Chiang 1998, personal communication). Smoke particles in this size range also follow the flow quite faithfully, so the same particles could be used for the PIV measurements. An estimate of the mean particle response time to a step change in velocity is about 5×10^{-7} s; the highest turbulent frequency in this flow as determined from velocity spectra, has a period of about 10^{-3} s. The Schmidt number for this type of smoke is very high – of the order of 10^6. As for the water flow experiment, the second CCD camera, facing the first, was zoomed to a smaller subfield of view so that the smoke particles could be individually imaged for PIV. The small time interval, Δt, between the two light sheets resulting from the pair of laser pulses was varied for this air flow experiment from 0.4 ms near the wall to 0.225 ms in the flow region above the obstacle, in order to take into account the different mean velocity zones.

The smoke was generated by smouldering coils of incense in a combustion chamber. Under slight pressure from a compressed air source, the smoke was passed through a filter to remove tar and large particles, through a heat exchanger to bring it to the temperature of the wind tunnel air and then through two screens stretched across a box, like the one used in the water flow experiment. These screens thoroughly mixed the smoke before it was released into the flow in the downstream direction through the slot. The slot, with a wall opening of approximately 1.5 mm, was curved in order to allow the smoke-laden air to enter the flow as nearly tangent to the wall as possible. With the boundary layer free-stream speed fixed at 2.3 m s^{-1} and the obstacle removed from the wall, the mean velocity of the smoke-filled air above the slot at $y^+ \approx 4$ was measured as $\overline{U} \approx 0.23$ m s^{-1} and $\overline{V} \approx 0.06$ m s^{-1}. Thus this measured $\overline{U}$ is somewhat lower at this location just above the slot compared to the flow without the slot. Of course, this is in the very high mean shear region of the viscous sublayer, and the particle displacements are very small. Thus these velocity measurements are subject to rather large errors. With the obstacle in place on the wall, these component mean speeds were $\overline{U} \approx 0.03$ m s^{-1} and $\overline{V} \approx 0.12$ m s^{-1}, respectively. The normalized source strength has been estimated to be $\overline{Q}^* \approx 7.8 \times 10^{-3}$.

For this air flow case the concentration field CCD camera also had a large field of view of about 120 mm × 80 mm in the horizontal and vertical directions, respectively. The PIV CCD camera was zoomed into a smaller subfield of the concentration field of view, approximately 10.5 mm × 7 mm corresponding to about $1h$ horizontally and $0.7h$ vertically. This PIV subfield needed to be smaller, and thus more highly resolved, than the subfield for the water experiment, because the smoke particles served a dual role in this case and had to be individually imaged for the PIV. As for the water channel experiment, an instantaneous realization of the field of view of the wind tunnel air flow concentration CCD camera is shown in the example video frame of figure 8(*a*). The obstacle is on the left, the high concentration of the incense smoke is just above and, at this instant, mainly upstream of the wall source and the subfield obtained with the zoomed PIV CCD camera is indicated. As before, the parts of the image above the plume and below the wall without useful information have been removed. Just as for the water flow experiment, this PIV subfield of view is further divided into a mesh of small subzones with dimensions of about $0.13h$ in the x- and $0.09h$ in the y-directions in which the local U and V velocity components are determined. The images of the smoke particles obtained in the PIV subfield and resulting from

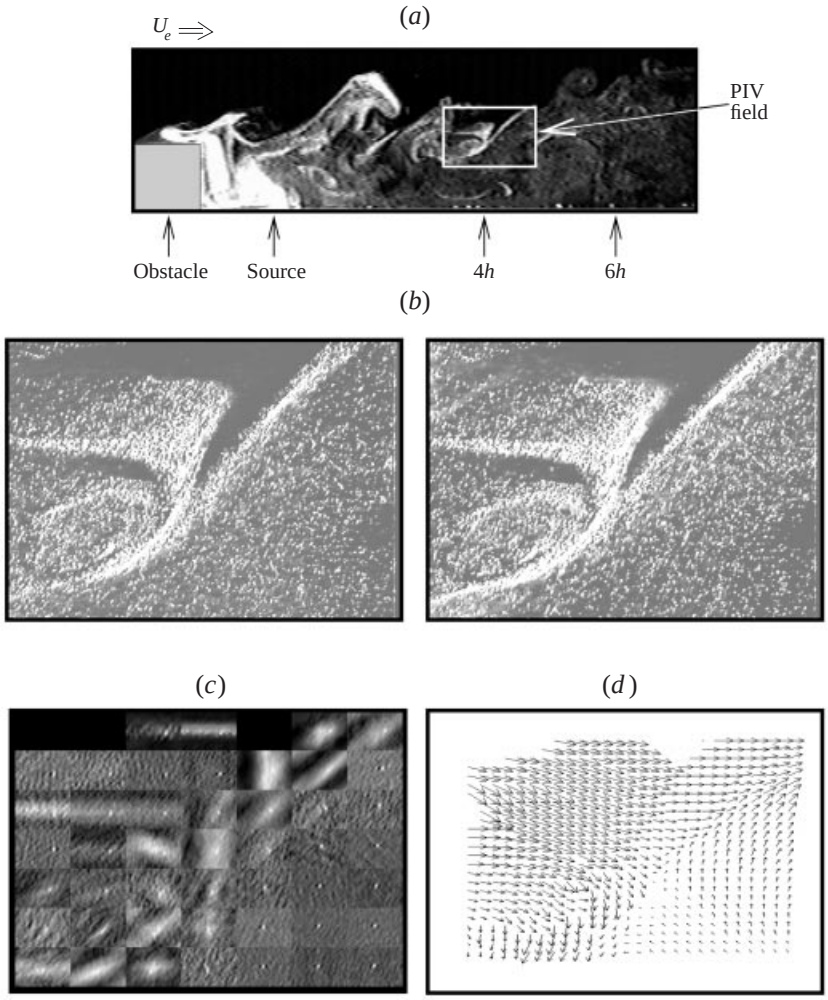

FIGURE 8. (*a*) Instantaneous video image of incense smoke scalar released from a line slot, 1*h* downstream of a square obstacle of cross-section h^2 located on the wall. Smoke particles are also imaged in the zoomed PIV subfield marked by the box in the figure. (*b*) Pair of PIV subfield images of smoke particles with Δt time separation. All such pairs are cross-correlated to determine the velocity components in the plane. (*c*) Correlation map. (*d*) Projection of the velocity vector field on the image plane.

a pair of pulses, separated by Δt, from the two YAG lasers are shown in part (*b*) of figure 8. The cross-correlation map showing the correlation peak in each of the 49 subzones (white dots) is shown in part (*c*), and the velocity component vector field resulting from this process for this example pair of images is shown in part (*d*). The additional vectors were obtained by overlapping the subzones as discussed for figure 3. The images in this example were taken at the edge of the plume. As seen in the figure, there are regions in the images where no smoke particles are found, and thus the velocity in these regions cannot be determined. This is reflected in the vector field of (*d*).

Only for the case of passive scalar dispersion of particles of a single diameter, i.e. monodispersed particles, is there a unique linear relationship between the light

intensity grey levels and particle concentration number density. As discussed in detail by Ayrault & Simoëns (1995), for the polydispersed incense particles of this experiment, the grey level of the scattered light is proportional to $\sum d_i^2 N_i$, where N_i is the number density of particles of diameter d_i, and the subscript i denotes the ensembles of different particle diameters in the total sample (here taken as the average diameters of a range of narrow bands). This is true provided the absorption of light along the optical path, geometrical distortions and background illumination effects have been accounted for, as they have been in the present case. However, in an investigation of the dispersion of polydispersed incense smoke from a wall line source in a flow like the present one, but without the obstacle on the wall, Wallace *et al.* (1995)) have been able to verify the linear relationship

$$\frac{\overline{C}_{eq}}{\overline{C}_{eq(max)}} \equiv \frac{d_{eq}^2 \overline{N}_{eq}}{d_{eq}^2 \overline{N}_{eq(max)}} \equiv \frac{\sum d_i^2 \overline{N}_i}{\sum d_i^2 \overline{N}_{i(max)}} \approx \overline{I}/\overline{I}_{max} \tag{2.3}$$

between the relative mean concentration for the monodispersion of ideal 'equivalent' particles of a single diameter, d_{eq} and the relative mean grey level of the light intensity from the polydispersed particles. Here the subscript notation 'max' denotes the maximum mean values of the light intensity and of the concentration number density in the illuminated plane. This sought linear relationship was clearly evident when they measured $\sum d_i^2 \overline{N}_i / \sum d_i^2 \overline{N}_{i(max)}$ with a laser aerosol spectrometer counter (PMS model LAC-236) that sorted and counted the particles in 16 narrow diameter bands, d_i, and plotted it against the $\overline{I}/\overline{I}_{max}$ relative light intensity mean grey levels recorded on film and digitized for image analysis. Furthermore, this relationship holds instantaneously as well as on average.

Wallace *et al.* (1995) demonstrated, therefore, that the distribution of relative grey levels of the scattered light, $\overline{I}/\overline{I}_{max}$, from the polydispersed incense smoke particles in the flows they and we have studied is the same as that which would have obtained in a monodispersed particle flow of constant particle size, d_{eq}, with a relative particle concentration number density given by $\overline{N}_{eq}/\overline{N}_{eq(max)}$, as indicated in (2.3). In addition, for the case where the polydispersed particle size distribution remains constant throughout the plume, the relative mean grey level measured, $\overline{I}/\overline{I}_{max}$, is also linearly related to the relative particle concentration number density, $\overline{C}_{eq}/\overline{C}_{eq(max)}$ (see Ayrault & Simoëns 1995). In summary, the measured relative instantaneous and mean grey levels in the experiment we carried out give relative concentration levels in the plume for two 'equivalent' experiments: one with monodispersed particles and the other with polydispersed particles that have a constant size distribution throughout the plume. In other words, for this type of incense smoke, a mapping exists that transforms the actual polydispersed experiment that was carried out into either of these two ideal experiments.

Unlike the water flow case, it was not possible to individually record the concentration images on separate frames because the time between the laser pulses was too short compared to the reception time required by the CCD camera to record an image. Therefore, the video recording rate of the concentration field CCD camera images was synchronized with the cycle rate of the two lasers so that their successive pulses for each cycle were superimposed on one frame. Because the time resolution of the velocity components is Δt, i.e. the time between pulses, this averaging of the concentration field images results in the same time resolution. We confirmed that the CCD camera linearly added the light intensity for each pixel resulting from the two pulses, provided that it was not saturated.

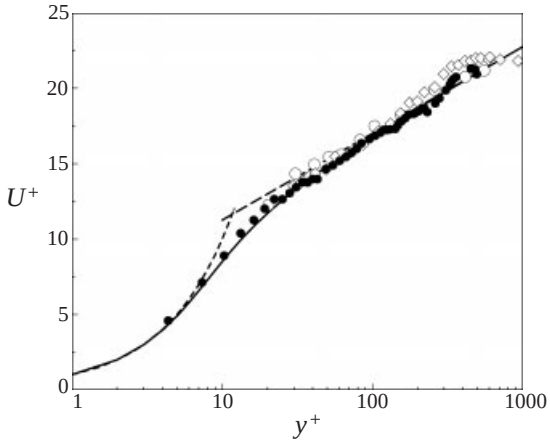

FIGURE 9. Mean velocity profile in the wind tunnel: open diamonds, present pitot tube data, $R_\theta = 1050$; open circles, present X-array hot-wire probe data, $R_\theta = 1050$; filled circles, present PIV data, $R_\theta = 980$; short dashes, $U^+ = y^+$; long dashes, $U^+ = 2.5 \ln y^+ + 5.5$; solid line, curve fit of Spalding (1961).

For the experiment in air, the same problem with the dynamic range of the concentration field CCD camera was encountered as for the water flow experiment. Therefore, as was done by Ayrault & Simoëns (1995), for each downstream measurement location of the camera, an $f^\# = 2.8$ aperture opening was chosen, by looking at the signal level on an oscilloscope, in order to obtain the maximum dynamic range without saturating. The camera aperture opening then was reduced to $f^\# = 16$, and the concentration field was re-recorded in order to obtain the light intensity at the source without saturation.

2.2.1. *Preliminary PIV measurements in the boundary layer without the obstacle*

As in the case of the water channel experiment, preliminary measurements were made to establish that the wind tunnel flat-plate boundary layer without the obstacle had standard statistical properties and that these properties could be measured with the PIV system that was later used for the flow with the obstacle. Pitot tube measurements and X-array hot-wire measurements of the mean velocity profile were made with a boundary layer free-stream speed of $2.5\,\mathrm{m\,s^{-1}}$ and $R_\theta = 1050$; they are compared in figure 9 to those obtained with the PIV system with a free-stream speed of $2.3\,\mathrm{m\,s^{-1}}$ and $R_\theta = 980$. Also shown in the figure is the logarithmic relation, $U^+ = 2.5 \ln y^+ + 5.5$, the linear relationship $U^+ = y^+$ and the curve fit of Spalding (1961). The PIV results are in excellent agreement with the pitot tube measurements in the logarithmic and buffer layers. The hot-wire measurements show slightly larger values of U^+ in the upper part of the logarithmic region. Both the pitot tube and hot-wire $\overline{U}$ values are normalized and y^+ is calculated with $u_\tau = 0.115\,\mathrm{m\,s^{-1}}$, which was iteratively determined by a Clauser fit of the measured values in the logarithmic layer.

The PIV r.m.s. values, u'^+ and v'^+, measured in the wind tunnel flow without the obstacle in place, are compared in figure 10 with our X-array hot-wire measurements and with the direct numerical simulation (DNS) values of Spalart (1988) for $R_\theta = 670$ and 1410. Our u'^+ PIV values also are in excellent agreement with both the hot-wire and DNS comparison data. The v'^+ values are also in good agreement except for the two points closest to the wall, where the local shear is high.

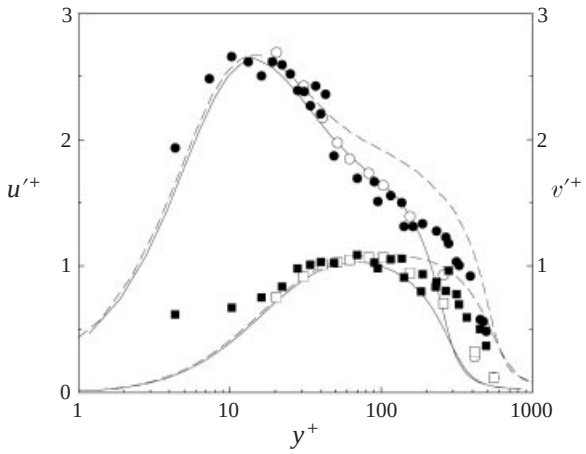

FIGURE 10. Root-mean-square velocity fluctuation profiles in the wind tunnel: circles, u'^+; squares, v'^+. Open symbols, present X-array hot-wire probe data, $R_\theta = 1050$; closed symbols, present PIV data, $R_\theta = 980$; solid lines, Spalart's (1988) DNS, $R_\theta = 670$ and dashed line, $R_\theta = 1410$.

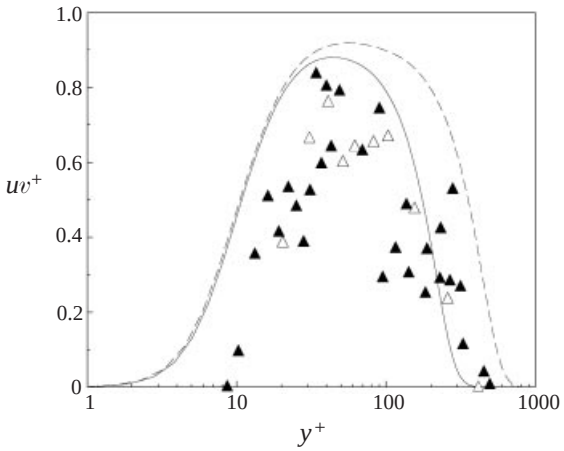

FIGURE 11. Reynolds shear stress profiles in the wind tunnel: open triangles, present X-array hot-wire probe data, $R_\theta = 1050$; closed triangles, present PIV data, $R_\theta = 980$; solid line, Spalart's (1988) DNS, $R_\theta = 670$ and dashed line, $R_\theta = 1410$.

Our PIV-determined Reynolds shear stress values are compared to our hot-wire measured values and the DNS values of Spalart (1988)) in figure 11. Our hot-wire and PIV measured values are considerably smaller than Spalart's DNS values at both simulation Reynolds numbers for $y^+ \leqslant 200$. The reason for this is unclear. The PIV measured values in this preliminary test display quite a lot of scatter, but the overall agreement with the hot-wire data is fairly good.

In summary, the preliminary experiments showed that both the water and air turbulent boundary layers, generated as the base flows for this study of passive scalar dispersion from a line source downstream of an obstacle on the wall, have reasonably standard velocity field statistical properties. Furthermore, they also showed that the mean and r.m.s. velocity values can be measured with the PIV system described above to a fairly good accuracy, provided the measurements are not made in regions where the mean shear is too large. To make such measurements in the high shear region it

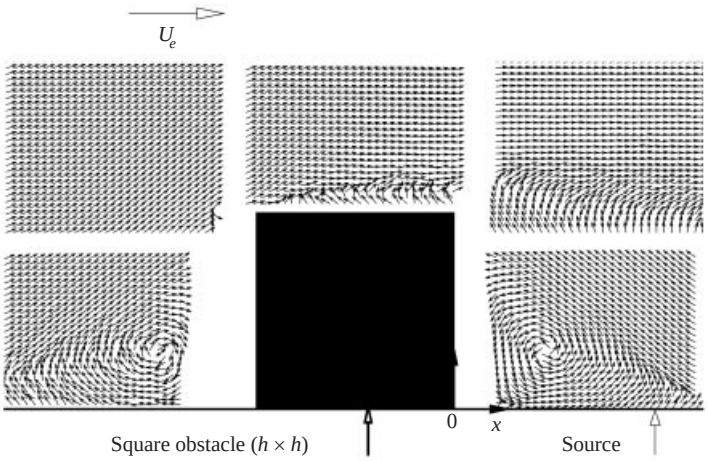

FIGURE 12. Mean velocity field around the square-section obstacle in the (x, y)-plane for the air experiment. The five zones correspond to five measurement stations of the PIV CCD camera.

is necessary to perform supplementary experiments with variation of the time step, Δt, between the two exposures. This is time consuming and was not necessary for the purposes of this investigation because, for the flow with the obstacle on the wall, the maximum mean shear at the three measurement locations occurs at $4h$ downstream of the obstacle, just above the level of the top of the obstacle in the mixing region between the recirculating zone and the outer flow. This mean shear is no greater than that at $y^+ \approx 20$ in the smooth-wall boundary layer with no obstacle. For $y^+ \geqslant 20$ in the smooth-wall boundary layers, the PIV measurements of u'^+ and v'^+ in the figures above are in reasonably good agreement with the hot-wire and DNS comparison results. For $y^+ \leqslant 60$, however, the PIV Reynolds shear stress results are in poorer agreement.

3. Results for flow over and downstream of a square obstacle on the wall

With the obstacles in place on the flat plates of the water channel and wind tunnel, the scalar concentration and the velocity components were simultaneously measured as described above in §§ 2.1 and 2.2. The video images were digitized and processed as described in the Appendix, resulting in (x, y)-plane concentration and velocity field information downstream of the obstacle in the recirulation region and above it in the mixing zone. Statistics of the velocity field will be shown for the vertical profiles at the $x = 4h$ and $6h$ locations. An additional set of data centred on $x = 20h$ was obtained in the wake region of the air flow that will be discussed in the context of the similarity analysis presented in § 3.6. For the $4h$ and $6h$ locations mean gradient transport models of the scalar fluxes, $\overline{uc}$ and $\overline{vc}$, and the momentum flux, $\overline{uv}$, are compared to the measurements. For the $20h$ location in the wake region, a similarity analysis is carried out and the results are also compared to the measurements.

3.1. *Velocity component measurements*

Before considering detailed statistical properties in the large downstream recirculation region, it is instructive to look at projections on the (x, y)-plane of the mean velocity vector fields of the flow in this region and upstream in the vicinity of the obstacle. The latter are shown in figure 12 for the air flow experiment. These mean velocity vectors

were determined from the procedure described in the Appendix in which the entire boundary layer was seeded with smoke in order to measure $\overline{U}_i$ throughout. In this figure a vortex with negative vorticity is clearly evident just upstream of the obstacle extending from near the wall up to about $0.6h$ above the obstacle and to about $1h$ upstream of it. Individual instantaneous vector fields revealed that this vortex is quite stationary.

A weaker vortex of about the same size with positive vorticity is seen just downstream of the obstacle. This vortex is also quite stationary. Scalar from the source slot becomes trapped in this vortex making it a region of high concentration.

A zone of high shear is evident above the obstacle with a region of some slow reverse flow between it and the obstacle. Near the downstream end of the figure the beginning of a much larger scale recirculation region is apparent. It is in this region, called 'the recirculation region' in this paper, that detailed statistical information has been obtained at $4h$ and $6h$ downstream of the obstacle.

The mean vector field in figure 12 indicates how scalar can be transported upstream from the source and over the top of the obstacle, as has happened in the instantaneous image in figure 8. The scalar is carried upward and back toward the obstacle between the two counter-rotating vortices, one small and just downstream of the obstacle and the other large and further downstream. Near the downstream top corner of the obstacle the scalar is picked up in the reverse flow there and is transported further upstream over the obstacle.

In figure 13 the downstream end of the large recirculation region is shown for the water flow between $x = 3.85h$ and $6.15h$ and in figure 14 for the air flow between $x = 3.5h$ and $6.5h$. The upstream end of this region was seen at the right-hand side of figure 12. A line along which the mean velocity is approximately zero delineates the upper extent of the recirculating region in the mean field. The point where the flow above the recirculating region reattaches to the wall appears to be at about $6.5h$ in both cases. As mentioned before, this reattachment location is close to the value of $7h$ found by Schofield & Logan (1990) for the same $\delta/h = 7$ ratio and is also close to the value of $6h$ found by Counihan *et al.* (1974) for $\delta/h = 8$.

In figure 15 $\overline{U}/U_e$ and $\overline{V}/U_e$ profiles for the mean velocity components, normalized by the external flow velocities, are shown to the same scale, respectively, for (*a*) the water flow up to $2.9h$ above the wall and for (*b*) the air flow, up to $2.1h$. For the air flow, above $2.1h$ there were not enough particles present to obtain concentration flux measurements, so all the air flow plots stop at this level. The wall-normal mean velocity values are quite small compared to the streamwise mean velocity values at both locations and for both flows. A region of mean flow directed upstream is quite evident at $4h$, up to about $0.6h$ above the wall. At $6h$ this reverse flow region is much smaller in the water flow and is barely apparent in the air flow profile. The upper extent of this reverse flow occurs at the lines of zero velocity in figures 13 and 14. In general, the mean velocity results are in good agreement for the two flow cases with different fluids and somewhat different Reynolds numbers. The $\overline{U}$ profiles for the two flows are in particularly good agreement at the respective downstream locations.

This agreement is shown even more clearly when $\overline{U}$ at $4h$ and $6h$ downstream of the obstacle is plotted in figure 16 in the form of a deficit velocity with respect to the mean velocity of the flow with no obstacle, $\Delta\overline{U} \equiv \overline{U} - \overline{U}_{bl}$. Here $\overline{U}_{bl}$ is the mean streamwise velocity in the boundary layer with no obstacle at the same vertical location as $\overline{U}$ in the obstacle flow, and the normalization is by the obstacle-free flow mean velocity at h above the wall, $\overline{U}_{bl}(h)$. The similarity of the mean velocity fields of the two flows is evident.

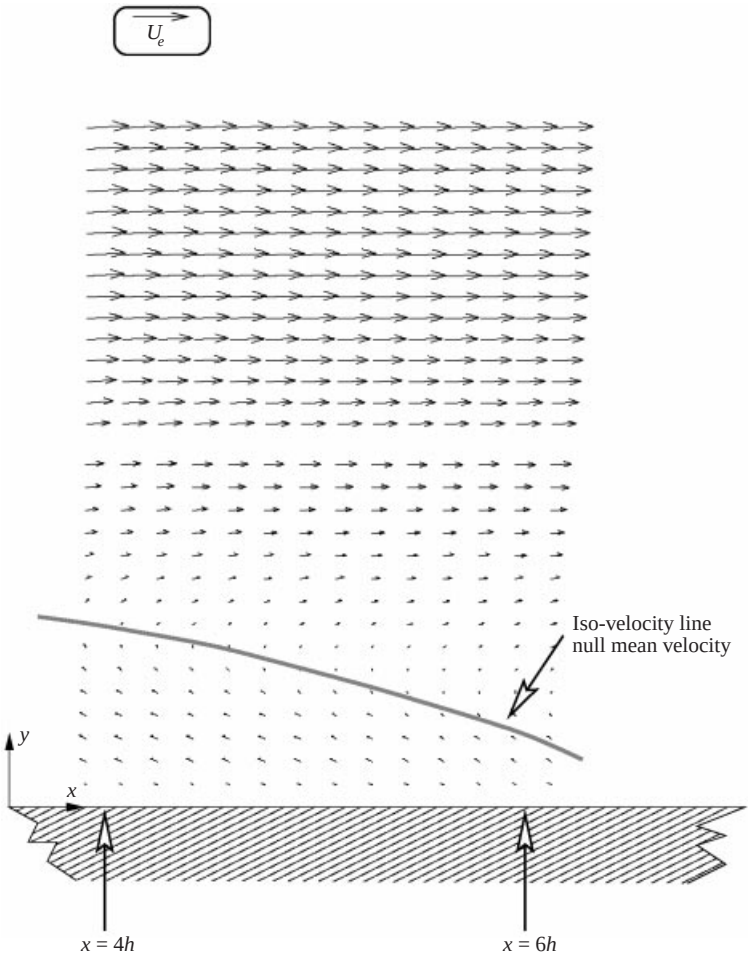

FIGURE 13. Mean velocity field in the recirculation zone downstream or the obstacle from $x = 3.85h$ to $x = 6.5h$ for the water flow experiment. The two zones correspond to two measurement stations of the PIV CCD camera.

The root-mean-square u'/U_e and v'/U_e profiles are shown in figure 17, at $4h$ and $6h$ downstream of the obstacle for (*a*) the water flow and (*b*) the air flow. The intensity of the v fluctuations is considerably less than the u fluctuations at both these x locations and in both fluid media. The maxima of the u'/U_e profiles occur in the vicinity of $1.2h$–$1.5h$ in the mixing region above the level of the obstacle and near the inflection points in the $\overline{U}$ profiles of figure 15 where the mean velocity gradient is largest. The maxima of the v'/U_e profiles also occur in the mixing region, but they are considerably less pronounced. In general, the agreement of the r.m.s. profiles for the two flows is reasonably good, although there are some differences in detail that can be attributed to PIV inaccuracies, as mentioned in § 1 and discussed in the Appendix. In addition, the difference in Reynolds numbers of the two flows probably has an effect in this range of low R_h.

The Reynolds shear stress profiles for these x locations and flows are plotted in figure 18. For both flows, $\overline{uv}/U_e^2$ values are everywhere negative and have larger magnitudes at the $6h$ location further downstream of the obstacle than at $4h$ for all y/h positions except very close to the wall. The negative values indicate that transport

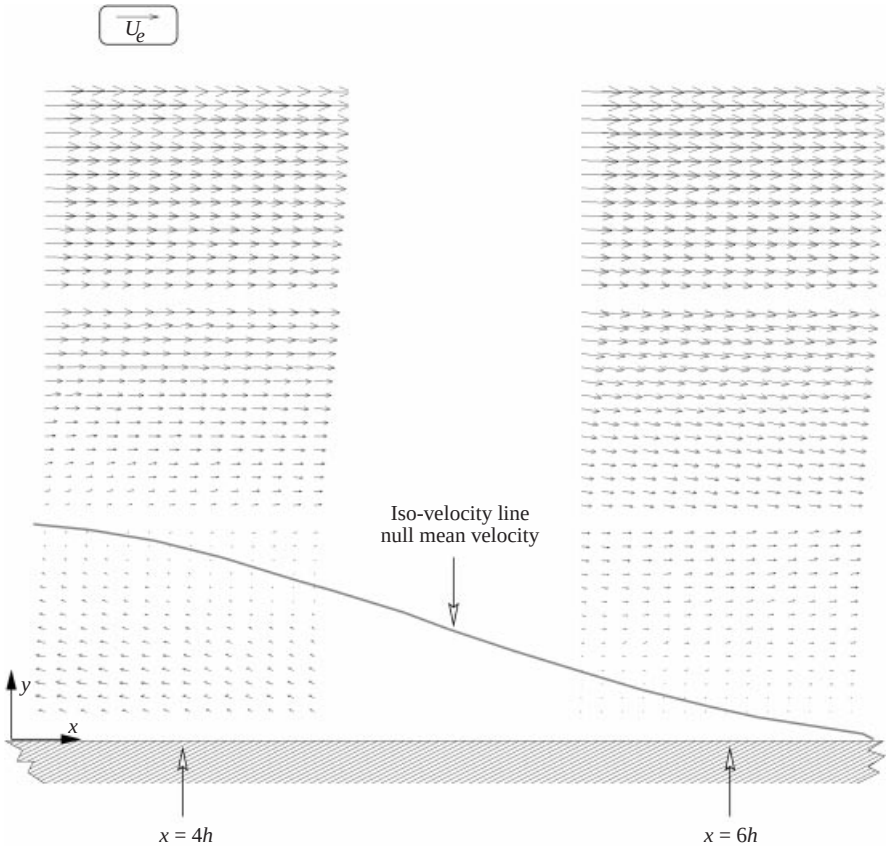

FIGURE 14. Mean velocity field in the recirculation zone downstream of the obstacle from $x = 3.5h$ to $x = 4.5h$ and from $x = 5.5h$ to $x = 6.5h$ for the air flow experiment. The six zones correspond to six measurement stations of the PIV CCD camera.

processes that produce $+u,-v$ and $-u,+v$ motions dominate this flow region just as they do for smooth-wall boundary layers. Such motions are of the mean gradient type, a point that will be discussed in detail in § 3.4 regarding the scalar concentration fluxes. The negative maxima occur in the mixing zone just above the level of the top of the obstacle, for both $4h$ and $6h$ and for both flows. In general, the $\overline{uv}/U_e^2$ profiles of the water and air flows agree with each other quite well, although there are some small differences in the magnitudes of the values.

3.2. *Concentration field measurements*

The light intensity of each respective pixel from the entire ensemble of 1000 images obtained with the concentration full field CCD camera were averaged. As discussed in § 2.2 the light intensity obtained at each pixel is proportional to the fluorescent dye concentration for the water flow and to the concentration number density of the monodispersed particles of an 'ideal' equivalent of the polydispersed smoke of the air flow in the region imaged by the pixel. The concentration fluctuations about these mean values are obtained from the differences between the light intensities of each pixel of the instantaneous images and their average values.

From full planar field images of the mean and r.m.s. concentration, profiles can be obtained and compared at locations previously determined to be outside the zone of

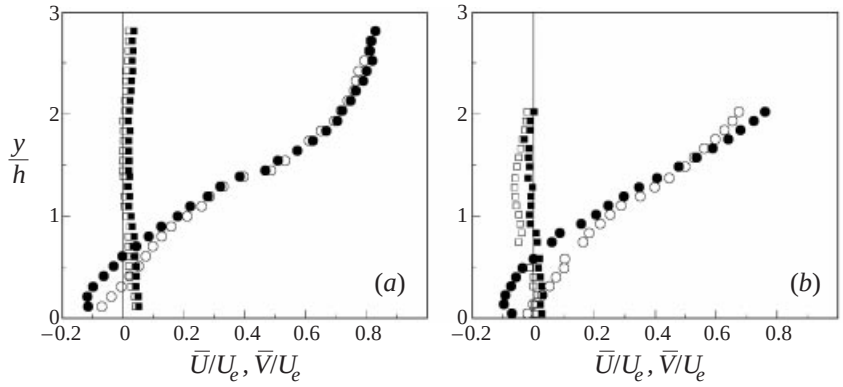

FIGURE 15. Mean velocity profiles downstream of a square rod obstacle on the wall of (*a*) water channel and (*b*) wind tunnel: closed circles, $\overline{U}$, and closed squares, $\overline{V}$, at $4h$; open circles, $\overline{U}$, and open squares, $\overline{V}$, at $6h$. U_e is the external flow velocity.

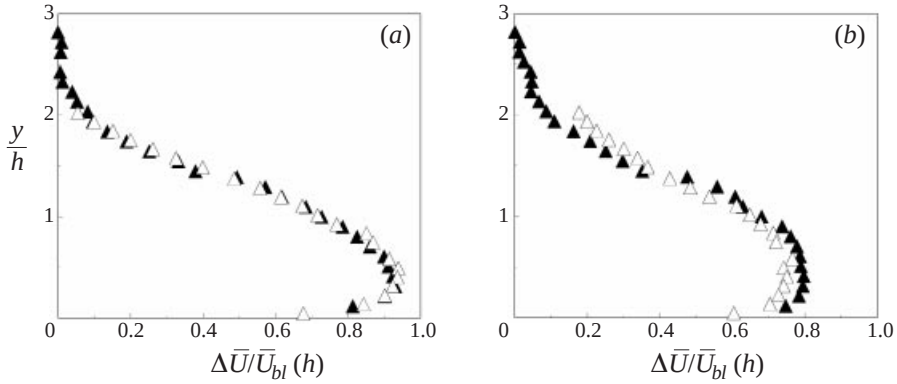

FIGURE 16. Mean streamwise deficit velocity profiles downstream of a square rod obstacle on the wall at (*a*) $x = 4h$ and (*b*) $x = 6h$: closed triangles, water flow; and open triangles, air flow. $\overline{U}_{bl}(h)$ is the mean velocity in the obstacle-free boundary layer at h above the wall.

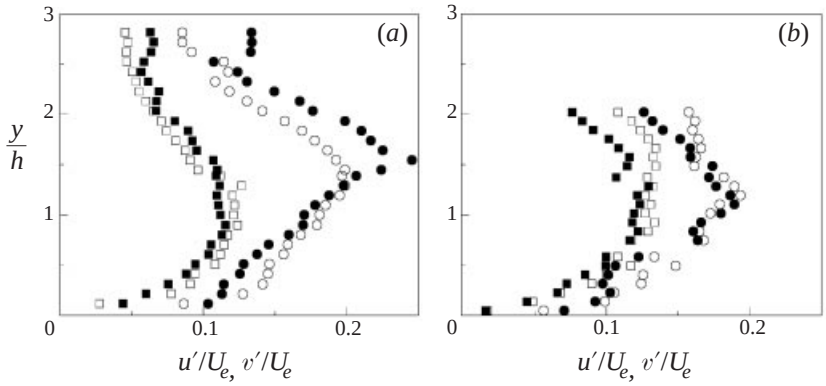

FIGURE 17. Root-mean-square velocity fluctuation profiles downstream of a square rod obstacle on the wall of (*a*) water channel and (*b*) wind tunnel: closed circles, u', and closed squares, v', at $4h$; open circles, u', and open squares, v', at $6h$. U_e is the external flow velocity.

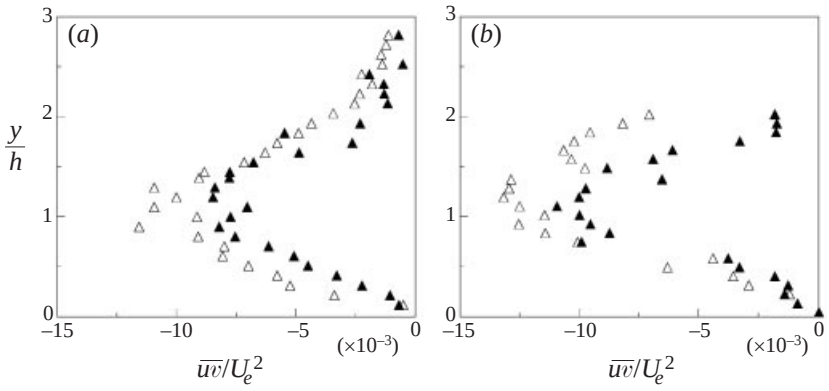

FIGURE 18. Reynolds shear stress profiles downstream of square rod obstacle on wall of (*a*) water channel and (*b*) wind tunnel: closed triangles at 4*h*, open triangles at 6*h*. U_e is the external flow velocity.

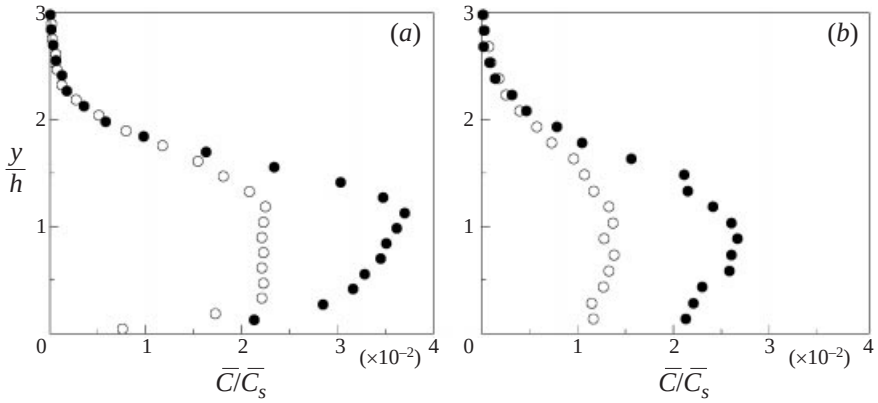

FIGURE 19. Vertical profiles of relative mean concentration, $\overline{C}/\overline{C}_s$, at 4*h* (closed circles) and 6*h* (open circles) downstream of the obstacle: (*a*) water boundary layer with dispersion of Rhodamine B, $Sc \approx 2500$, and (*b*) air boundary layer with dispersion of incense smoke, $Sc \approx 10^6$.

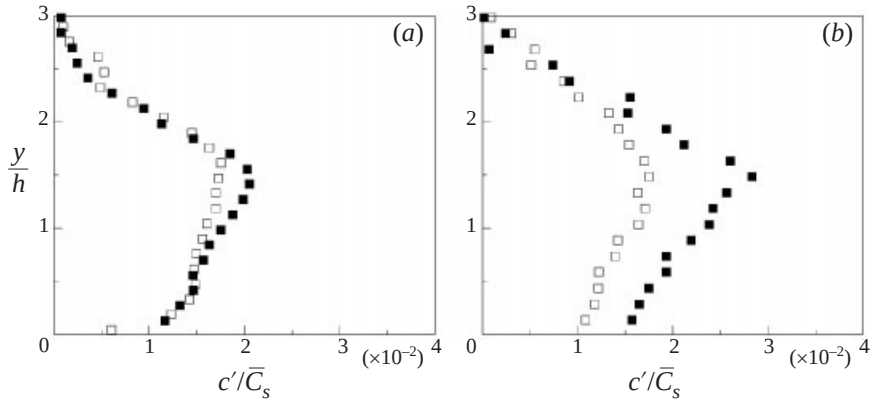

FIGURE 20. Vertical profiles of relative root-mean-square concentration, $c'/\overline{C}_s$, at 4*h* (closed squares) and 6*h* (open squares) downstream of the obstacle: (*a*) water boundary layer with dispersion of Rhodamine B, $Sc \approx 2500$, and (*b*) air boundary layer with dispersion of incense smoke, $Sc \approx 10^6$.

CCD camera saturation. In figure 19(*a*) the vertical profiles of $\overline{C}/\overline{C}_s$ at $x = 4h$ and $6h$ are shown for the water flow and in (*b*) for the air flow. In the water flow at $4h$, the peak concentration occurs just above the top of the obstacle level at $y/h \approx 1.2$, but in the air flow this peak is slightly below this level at $y/h \approx 0.9$. These $\overline{C}/\overline{C}_s$ profiles in the recirculating zone are flatter at $4h$ than at $6h$. The maximum values of $\overline{C}/\overline{C}_s$ are about 3.8% of the source value at $4h$ for Rhodamine B in water, but only 2.7% for incense smoke in air. These maxima are significantly reduced at $6h$ to about 2.2% and 1.4%, respectively. For both flows and for both x locations the mean plume extends to about $y/h \approx 3.0$, i.e. far above the recirculation region that was seen in figure 15 to extend up to about $y = 0.6h$ at $x = 4h$ and $0.2h$ at $x = 6h$. As discussed previously when considering figure 12, the scalar is transported up into the mixing region by the counter-rotating vortices located downstream of the obstacle, and then it is carried downstream, all the while being dispersed both outward and inward. Thus the scalar plumes grow, and their mean concentration profiles become more uniform with smaller peak values with increasing distance downstream.

The root-mean-square relative concentration profiles, $c'/\overline{C}_s$, at $4h$ and $6h$ are shown in figure 20(*a*) for the air flow and in (*b*) for the water flow. In both flows and at both x locations the peak r.m.s. concentration fluctuations occur at $y/h \approx 1.5$, although the profiles at $6h$, where the transported scalar is more dispersed, are more uniform and the maximum values are smaller than at $4h$. These peaks are in the mixing zone above the recirculating zone, just above the level of highest mean shear. Although the forms of the c' profiles are similar for the two media and the two scalars, the magnitude of the values is somewhat different. The peak r.m.s. value at $4h$ for the air flow with incense smoke is about 2.8% of the mean concentration at the source slot exit, $\overline{C}_s$. For the water flow with Rhodamine B fluorescent dye, this value is about 2.1%. However, the peak values of c' at $6h$ are about 1.7% of $\overline{C}_s$ for both flows. These differences and the differences in the mean values seen in figure 19 must be due to the different values of the three flow parameters of (1.2): Re_h, Sc and $\overline{Q}^*$, in addition to differences resulting from measurement errors.

3.3. *Concentration flux measurements*

The principal aim of this experimental investigation was to measure the scalar concentration fluxes, $\overline{uc}$ and $\overline{vc}$ in the complex flow downstream of a two-dimensional obstacle on the wall of a boundary layer, with a line source slot at the wall emitting the scalar. As described above, obtaining these quantities required the simultaneous measurements of the scalar concentration and the velocity vector fluctuations using flow visualization and optical techniques. Profiles of the $\overline{uc}$ fluxes at $4h$ and $6h$, where the values have been normalized by U_e and $\overline{C}_s$, are given in figure 21(*a*) for the water flow and in (*b*) for the air flow. Similarly, the $\overline{vc}$ profiles are given in figure 22(*a*, *b*). Above $y/h \approx 0.8$ the $\overline{uc}/U_e\overline{C}_s$ values are negative, and below this level they are positive for both flows and for both x locations. The $\overline{vc}/U_e\overline{C}_s$ values also change sign, from negative below $y/h \approx 0.7$ to positive above this level, for the water flow with Rhodamine B dye dispersion at $4h$. For the air flow with incense smoke dispersion, this change of sign of $\overline{vc}/U_e\overline{C}_s$ at $4h$ is near the level of the top of the obstacle, but there is a lot of scatter in the data in this region. Both flows have only small negative values of $\overline{vc}/U_e\overline{C}_s$ in the lower half of the recirculating zone for $6h$. The magnitudes of the $\overline{uc}/U_e\overline{C}_s$ fluxes are similar for the two flows, but the magnitudes of the $\overline{vc}/U_e\overline{C}_s$ fluxes are smaller for the water flow than for the air flow. The peak values of the $\overline{uc}/U_e\overline{C}_s$ fluxes occur at or just above $y/h = 1.5$ for both flows and x locations. The peak values of the $\overline{vc}/U_e\overline{C}_s$ fluxes are also at about the $y/h \approx 1.5$ level except for the

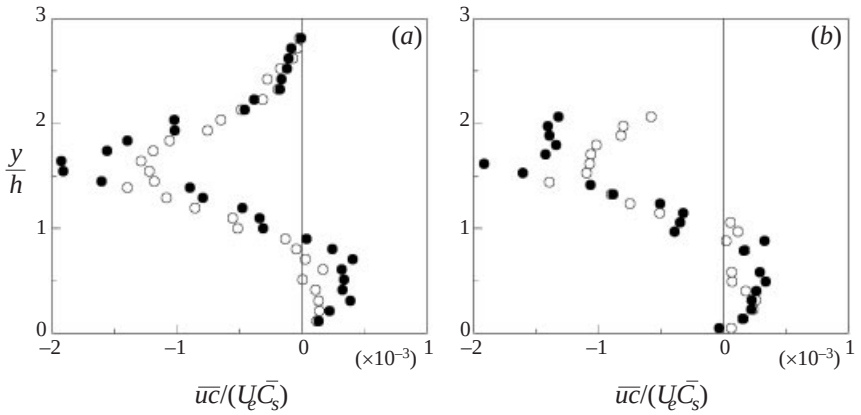

FIGURE 21. Vertical profiles of streamwise scalar flux, $\overline{uc}$, at $4h$ (closed circles) and $6h$ (open circles) downstream of the obstacle in (*a*) water channel with dispersion of Rhodamine B, $Sc \approx 2500$, and in (*b*) wind tunnel with dispersion of incense smoke, $Sc \approx 10^6$. The flux values are normalized by the product of the free-stream velocity, U_e, and the mean concentration at the source slot exit, $\overline{C}_s$.

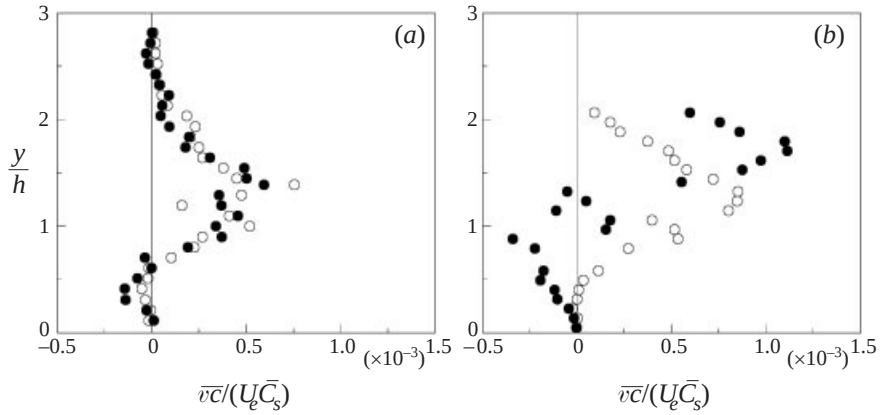

FIGURE 22. Vertical profiles of wall normal scalar flux, $\overline{vc}$, at $4h$ (closed circles) and $6h$ (open circles) downstream of the obstacle in (*a*) water channel with dispersion of Rhodamine B, $Sc \approx 2500$, and in (*b*) wind tunnel with dispersion of incense smoke, $Sc \approx 10^6$. The flux values are normalized by the product of the free-stream velocity, U_e, and the mean concentration at the source slot exit, $\overline{C}_s$.

$4h$ profile for the air flow. Here the peak values occur somewhat higher at $y/h \approx 1.8$. The reason for this anomalous upward shift of the profile is at present unclear.

The integrated total scalar flux across vertical planes should remain constant, neglecting the very small net viscous diffusion of the scalar across these profile planes. This constancy was checked for the $4h$ and $6h$ planes. For the water flow the flux was lower by about 16% at the downstream location and for the air flow this error was about 17%. These estimations of the integrated fluxes are subject to large uncertainties, because of the difficulty of curve fitting the scattered experimental data and because the air flow scalar fluxes could not be measured above $y/h = 2.1$.

Clearly the scalar fluxes are largest in the high-shear-layer mixing zone above the level of the top of the obstacle where the gradients of the mean velocity and mean concentration, $\partial\overline{U}/\partial y$ and $\partial\overline{C}/\partial y$, are at their maximum values. This zone is along the top of the large-scale recirculation eddy where the high shear layer occurs between

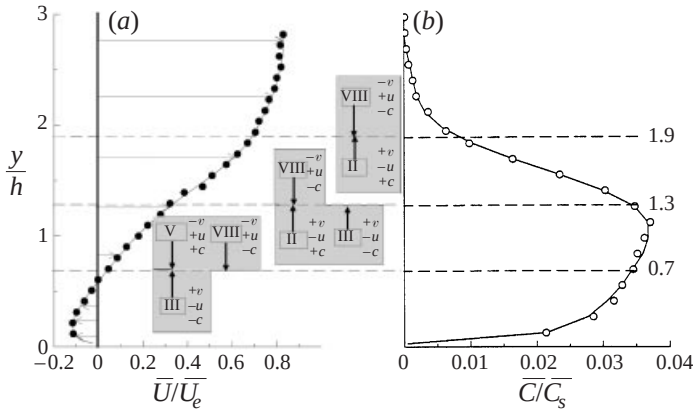

FIGURE 23. Sketch showing which scalar flux conditional categories (octants) correspond to mean gradient scalar transport type motions. The mean velocity profile for the water channel flow at $4h$ downstream of obstacle is replotted on the left and the mean concentration profile on the right. The levels $y/h = 1.9$, 1.3 and 0.7 are in the outer flow, mixing and recirculating zones, respectively.

I: $+u$, $+v$, $+c$	V: $+u$, $-v$, $+c$
II: $-u$, $+v$, $+c$	VI: $-u$, $-v$, $+c$
III: $-u$, $+v$, $-c$	VII: $-u$, $-v$, $-c$
IV: $+u$, $+v$, $-c$	VIII: $+u$, $-v$, $-c$

TABLE 1. Eight scalar flux conditional categories (octants) based on the sign combinations of $\pm u$, $\pm v$ and $\pm c$.

it and the boundary layer flow above. The turbulence intensities are also high in this region. These fluctuations efficiently mix the scalar that is transported upward from the source and then is carried downstream into this region.

3.4. *Conditional analysis of concentration fluxes*

In order to gain greater insight into the nature of the scalar transport processes in the flow region downstream of the obstacle that result in the $\overline{uc}$ and $\overline{vc}$ flux values, a conditional analysis of these fluxes at the $4h$ location downstream of the obstacle for the water flow experiment was carried out. As discussed in the Appendix, the scalar fluxes, $\overline{u_i c}$, can be determined even in regions of the flow where smoke particles are instantaneously sometimes not present. However, because the instantaneous velocity components cannot be determined in these instances, the type of conditional analysis described in this section is not possible for the air flow experiment.

The uc and vc product values at each time step of the data sample were sorted into the eight categories (octants) given by the sign combinations of the three variables, $\pm u$, $\pm v$ and $\pm c$, as defined in table 1. This sorting is an extension of the quadrant analysis of Wallace, Eckelmann & Brodkey (1972).

Reference to figure 23 aids in interpreting the conditional averages $\langle uc \rangle_{oct}$ and $\langle vc \rangle_{oct}$ in these octants. In this figure the mean velocity and mean concentration profiles resulting from the Rhodamine B dye released through the line source slot on the wall, for the water channel flow at $4h$, have been replotted. Three levels, $y/h = 1.9$, 1.3 and 0.7, have been chosen as representative of the three major zones of this flow downstream of the obstacle. These zones are the outer flow zone, the mixing

zone and the recirculating zone, respectively. The characteristics of the mean velocity and concentration profiles in the outer flow zone just above the mixing zone at the $y/h = 1.9$ level are similar to those of a boundary layer flow with scalar released at the wall, but with no obstacle upstream. The mean velocity increases monotonically and the mean concentration decreases monotonically with increasing distance from the wall. At this level, octants II and VIII correspond to scalar transport processes that can be approximated by a mean gradient type model. That is, if a fluid particle moves vertically upward ($+v$) to the 1.9 level from below while carrying and conserving the mean streamwise momentum and the mean concentration of its starting level, it will arrive with a deficit of momentum ($-u$) and an excess of concentration ($+c$) compared to the mean values at the 1.9 level. This type of transport has signs of the three variables like those of Octant II. Similarly, particles starting from above that move vertically downward ($-v$) to the $y/h = 1.9$ level also correspond to mean gradient transport if they carry and conserve their mean streamwise momentum ($+u$) and concentration ($-c$) from their location of origin until they arrive. This type of gradient transport approximates that of the scalar transport of the particle motions in octant VIII. The other six octants represent countergradient transport motions at this level.

Level $y/h = 1.3$ is in the lower part of the mixing zone just above the level of the top of the obstacle. In this zone the mean velocity and concentration gradients and the concentration fluxes reach their maximum values. Here, the scalar transport by the particle motions of octants II and VIII can also be represented by mean gradient transport. However, at this level octant II motions only are approximated by mean gradient transport for particles that start from below at a level with a mean concentration greater than that at the 1.3 level (i.e., that start their upward motion above approximately the 0.7 level). Particles starting from below the 1.3 level but with a mean concentration less than that at the 1.3 level (i.e. below approximately the 0.7 level) are also represented by mean gradient transport, but this type is that of octant III.

The $y/h = 0.7$ level is just at the top of the recirculation zone with reverse flow below $y/h \approx 0.6$ near the wall. Here similar considerations show that octants III, V and VIII are the three that contain particle motions that can be represented by mean gradient transport. At both the 1.3 and 0.7 levels the other five remaining octants correspond to countergradient transport type motions.

In figure 24 three types of octant-averaged normalized quantities are plotted. The three parts of the figure on the left are related to the $\overline{uc}$ flux, and the three parts on the right to $\overline{vc}$. In part (a) the fractional contributions to these fluxes of the motions in each octant, $\overline{uc}_{oct}/\overline{uc}$ and $\overline{vc}_{oct}/\overline{vc}$, are plotted for the three y/h positions. At each position the sum of the eight octant fractional values for each flux equals unity. The octants that can be represented by mean gradient scalar transport, as illustrated in figure 23, are indicated by larger symbols than for the other octants. Part (b) of figure 24 represents the fraction of the total sample time, t_{oct}/t, at each y/h position for which the uc and vc products reside in each of the octants. The resident time in each octant is, by definition, the same for both fluxes. The horizontal lines in the two parts of (b) are at the 0.125 level, i.e. the resident time fraction in each octant if the resident times were all equal. The sum over the octants for each flux is also unity for this octant resident time variable. Finally, in (c) the uc and vc instantaneous products averaged over just their resident time in each of the octants are shown. These values have been normalized by the constant flux scale, $U_e\overline{C}_s$, and they represent the intensity of the scalar transport by the motions of each of the octant categories.

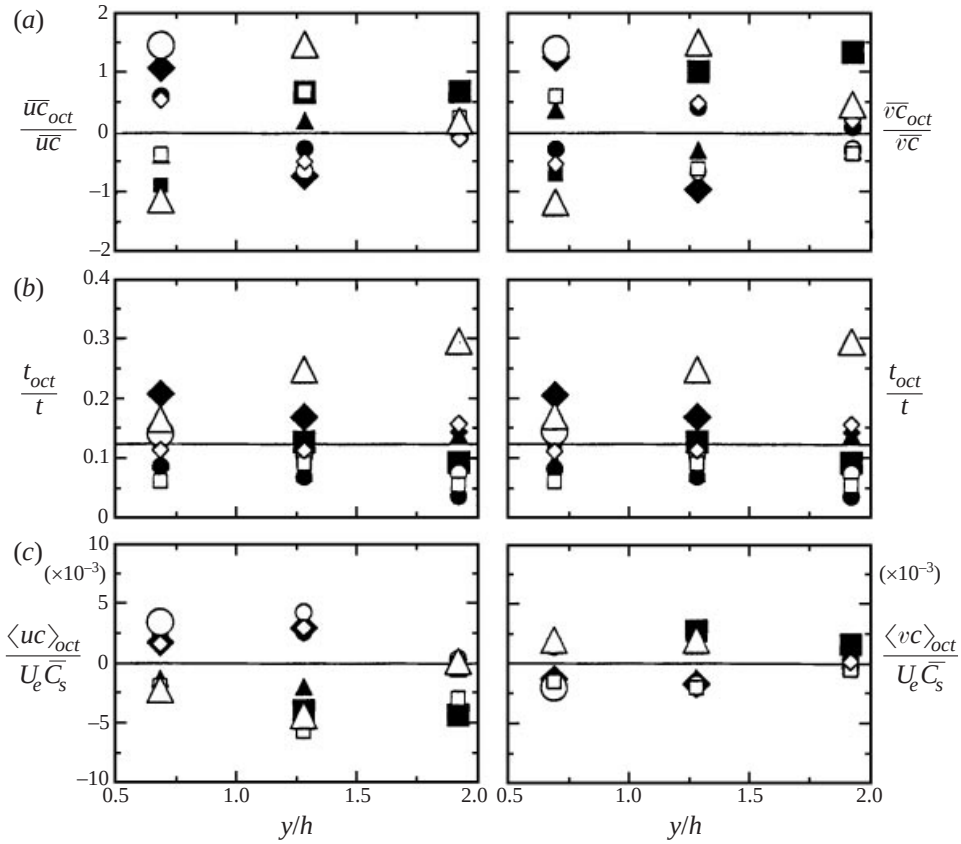

FIGURE 24. Octant conditional averages of normalized quantities related to the scalar fluxes, $\overline{uc}$ and $\overline{vc}$. Oct I: $+u, +v, +c$, filled circles; Oct II: $-u, +v, +c$, filled squares; Oct III: $-u, +v, -c$, filled diamonds; Oct IV: $+u, +v, -c$, filled triangles; Oct V: $+u, -v, +c$, open circles; Oct VI: $-u, -v, +c$, open squares; Oct VII: $-u, -v, -c$, open diamonds; VIII: $+u, -v, -c$, open triangles. (*a*) Fractional contribution of motions included in each octant, $\overline{uc}_{oct}/\overline{uc}$ and $\overline{vc}_{oct}/\overline{vc}$, where sum over octants for each flux is unity. (*b*) Fraction of total sample time, t_{oct}/t, at each y/h position that uc and vc products, respectively, reside in each of the octants. Horizontal line in subfigures of (*b*) are at the 0.125 level, i.e. the resident time fraction in each octact if resident times are all equal. Sum over octants for each flux is also unity in (*b*). (*c*) Subfigures show uc and vc products averaged over just their resident time in each octant. These values have been normalized by constant flux scale, $U_e\overline{C}_s$, and indicate intensity of scalar transport motions represented by each of the octant categories. The levels $y/h = 1.9$, 1.3 and 0.7 are in the outer flow, mixing and recirculating zones, respectively.

In the outer flow zone at $y/h = 1.9$ the contributions to both the $\overline{uc}$ and $\overline{vc}$ fluxes come principally from octant II, i.e. motion of particles from below carrying an excess of scalar and a deficit of momentum that can be approximated by mean gradient transport. Octant VIII, which also can be approximated by mean gradient transport motion, is the second largest contributor to the $\overline{vc}$ flux, but this contribution is significantly smaller than that of octant II. At this level countergradient transport contributions to the total fluxes are quite small. The dominance at this level of the octant II contributions to the fluxes is principally a result of the intensity of this type of transport, as is evident from parts (*b*) and (*c*) of figure 24. The resident time in octant II is only about 10%, indicating that this type of transport is not only intense, but quite intermittent in the outer zone. The uc and vc product signals reside in octant

VIII about 30% of the time, which is by far the longest resident time at this level and is the reason for its somewhat elevated contribution to the $\overline{vc}$ flux.

The situation changes somewhat in the mixing zone at $y/h = 1.3$. Here as well, octants II, III and VIII, which can be approximated by mean gradient transport, make the largest contributions to both $\overline{uc}$ and $\overline{vc}$, with octant VIII the greatest of these. However, the contributions of octants corresponding to countergradient transport type motions are not insignificant. The dominance of octant VIII motions, i.e. transport from above of an excess of momentum and a deficit of scalar, is a result of both the long resident time in this octant of about 25%, as seen in part (*b*) of figure 24, and the intensity of the fluxes, as seen in part (*c*). The intensity of octant II motion fluxes are similar to those of octant VIII, but the resident time in this category is much less. Octant III motions, which make an opposite-signed contribution to $\overline{uc}$ and $\overline{vc}$, are the result of somewhat elevated both resident time and intensities.

The motions in octants III, V and VIII, which can be approximated by mean gradient transport, also are the greatest contributors to both the $\overline{uc}$ and $\overline{vc}$ fluxes just at the top of the recirculating zone at $y/h = 0.7$, as seen in part (*a*) of figure 24. However, the contributions of the other octants, corresponding to countergradient transport, are not small – particularly that of octant II. The largest contributor to the fluxes is from octant V, representing particle motion from above the 0.7 level transporting both an excess of momentum and of scalar. This octant V type of flux is fairly intermittent, as seen in part (*b*) of figure 24. Its resident time is less than 15%. Its dominant contribution to the two fluxes is largely a result of its intensity – particularly for the $\overline{uc}$ flux. The octant VIII motions make opposite-signed contributions to $\overline{uc}$ and $\overline{vc}$ compared to the octant III and V motions.

In summary, it is clear that scalar transport by particle motion that can be approximated by a mean gradient model provides the dominant contributions to the fluxes in all three zones of the flow behind the obstacle. However, in the mixing and recirculating zones, fluid particle motions that are of the counter mean gradient transport type provide contributions to these fluxes that are not negligible. The net fluxes can be represented by mean gradient models, however, in all three zones.

3.5. *Second-order mean gradient models of scalar fluxes in the recirculation and mixing regions*

For a two-dimensional mean flow with small mean cross-stream velocity and, following local isotropy arguments of Wyngaard (1981), viscous terms assumed negligible, the evolution equations for the Reynolds stress $\overline{uv}$ and for the scalar fluxes $\overline{uc}$ and $\overline{vc}$ are

$$\frac{\partial \overline{uv}}{\partial t} + \overline{U}\,\frac{\partial \overline{uv}}{\partial x} = -\overline{uv}\frac{\partial \overline{U}}{\partial x} - \left(\overline{v^2}\,\frac{\partial \overline{U}}{\partial y} - \frac{\partial \overline{u^2 v}}{\partial x}\right) - \frac{\partial \overline{uv^2}}{\partial y} - \frac{1}{\rho}\left(\overline{v\,\frac{\partial p}{\partial x}} + \overline{u\,\frac{\partial p}{\partial y}}\right), \tag{3.1}$$

$$\frac{\partial \overline{uc}}{\partial t} + \overline{U}\,\frac{\partial \overline{uc}}{\partial x} = -\overline{u^2}\frac{\partial \overline{C}}{\partial x} - \overline{uv}\,\frac{\partial \overline{C}}{\partial y} - \overline{uc}\,\frac{\partial \overline{U}}{\partial x} - \left(\overline{vc}\,\frac{\partial \overline{U}}{\partial y} - \frac{\partial \overline{u^2 c}}{\partial x}\right) - \frac{\partial \overline{uvc}}{\partial y} - \frac{1}{\rho}\,c\,\overline{\frac{\partial p}{\partial x}} \tag{3.2}$$

and

$$\frac{\partial \overline{vc}}{\partial t} + \overline{U}\,\frac{\partial \overline{vc}}{\partial x} = -\overline{v^2}\frac{\partial \overline{C}}{\partial y} - \left(\overline{uv}\,\frac{\partial \overline{C}}{\partial x} - \frac{\partial \overline{v^2 c}}{\partial y}\right) - \frac{\partial \overline{uvc}}{\partial x} - \frac{1}{\rho}\,c\,\overline{\frac{\partial p}{\partial y}}. \tag{3.3}$$

If, further, the triple correlation terms are neglected and the mean properties are assumed approximately homogeneous in the streamwise direction, these equations

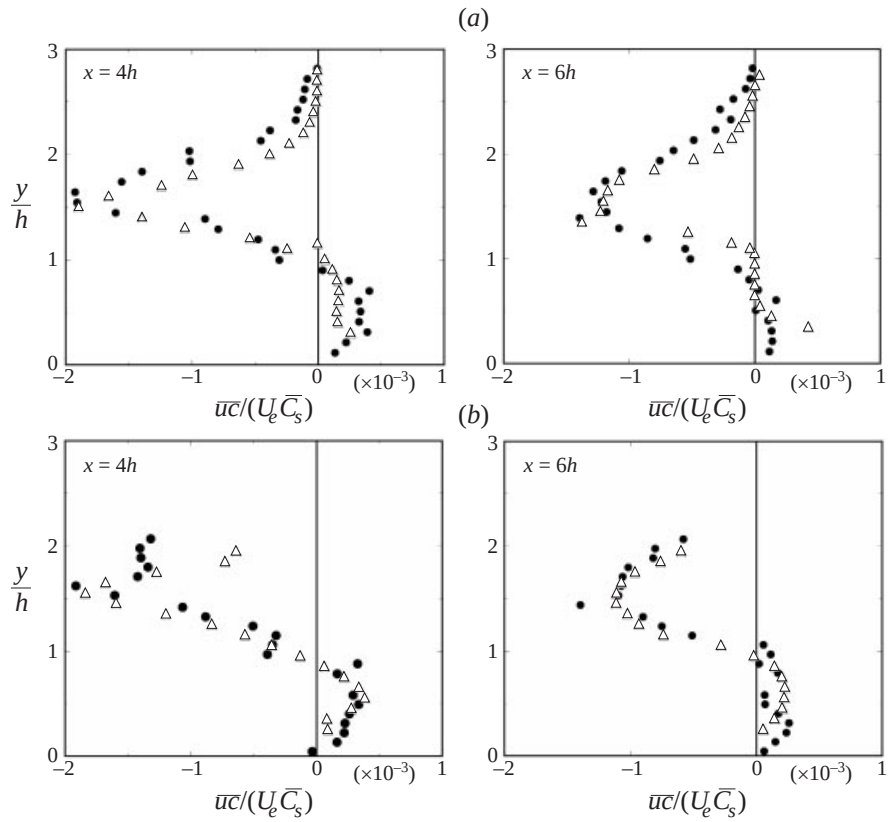

FIGURE 25. Vertical profiles of streamwise scalar flux downstream of the obstacle. Comparisons between direct measurements and second-order gradient model equation (3.12). Filled circles, $\overline{uc}$ from measurements; open triangles from model. (*a*) Rhodamine B dispersion in water, $Sc \simeq 2500$ and (*b*) smoke dispersion in air, $Sc \simeq 10^6$. $\overline{C}_s$ is the source mean concentration and U_e is the external flow velocity.

reduce to

$$\frac{\partial \overline{uv}}{\partial t} = -\overline{v^2}\,\frac{\partial \overline{U}}{\partial y} - \frac{1}{\rho}\left(\overline{v\,\frac{\partial p}{\partial x}} + \overline{u\,\frac{\partial p}{\partial y}}\right), \tag{3.4}$$

$$\frac{\partial \overline{uc}}{\partial t} = -\overline{uv}\,\frac{\partial \overline{C}}{\partial y} - \overline{vc}\,\frac{\partial \overline{U}}{\partial y} - \frac{1}{\rho}\,\overline{c\,\frac{\partial p}{\partial x}} \tag{3.5}$$

and

$$\frac{\partial \overline{vc}}{\partial t} = -\overline{v^2}\frac{\partial \overline{C}}{\partial y} - \frac{1}{\rho}\,\overline{c\,\frac{\partial p}{\partial y}}. \tag{3.6}$$

It should be noted that calculating the streamwise scalar flux, $\overline{uc}$, requires modelling both the momentum flux, $\overline{uv}$, and the cross-stream scalar flux, $\overline{vc}$. Because the mean turbulent field is stationary, the left-hand sides of (3.4), (3.5) and (3.6) are zero, leaving production of these fluxes by the mean velocity and concentration gradient terms in balance with their destruction by the pressure gradient terms, as Wyngaard (1981) pointed out in the context of discussing the modelling of the momentum and scalar fluxes for the neutral atmospheric surface layer. Moeng & Wyngaard (1989) have used the simple 'return to isotropy' model of Rotta (1951) to express the pressure

gradient terms in (3.4) and (3.6) as

$$\frac{1}{\rho}\left(\overline{v\frac{\partial p}{\partial x}}+\overline{u\frac{\partial p}{\partial y}}\right)=\frac{\overline{uv}}{\tau_1} \tag{3.7}$$

and

$$\frac{1}{\rho}\left(\overline{c\frac{\partial p}{\partial y}}\right)=\frac{\overline{vc}}{\tau_2}, \tag{3.8}$$

where τ_1 and τ_2 represent large-eddy turnover time scales. In like manner to (3.8) the pressure gradient–concentration correlation in (3.5) can be expressed as

$$\frac{1}{\rho}\left(\overline{c\frac{\partial p}{\partial x}}\right)=\frac{\overline{uc}}{\tau_3}. \tag{3.9}$$

Thus simple mean gradient models for $\overline{uv}$ and $\overline{vc}$ can be formulated as

$$\overline{uv}=-K_v\frac{\partial\overline{U}}{\partial y}\equiv-\tau_1\overline{v^2}\frac{\partial\overline{U}}{\partial y} \tag{3.10}$$

and

$$\overline{vc}=-K_s\frac{\partial\overline{C}}{\partial y}\equiv-\tau_2\overline{v^2}\frac{\partial\overline{C}}{\partial y}, \tag{3.11}$$

where the turbulent eddy diffusivity coefficients, K_v and K_s, are defined as the products of the time scales with the cross-stream velocity fluctuation variance, $\overline{v^2}$. Substituting the model expressions given in (3.9,) (3.10) and (3.11) into (3.5), the streamwise scalar flux, $\overline{uc}$ can be expressed in terms of the mean velocity and concentration gradients as

$$\overline{uc}=\tau_3(K_s+K_v)\frac{\partial\overline{U}}{\partial y}\frac{\partial\overline{C}}{\partial y}\equiv D_1\frac{\partial\overline{U}}{\partial y}\frac{\partial\overline{C}}{\partial y}, \tag{3.12}$$

where the transport coefficient, D_1, is the product of the sum of the eddy diffusivity coefficients in (3.10) and (3.11) with the time scale, τ_3. It has dimensions of length squared and can be viewed as a mixing length.

Some of the assumptions made above appear to be rather strong for this complex flow case, which includes the recirculation and mixing regions. On the other hand, the octant analysis in § 3.4 showed that the scalar fluxes have a good likelihood of being described well by mean gradient transport models. This is borne out when the measured values of $\overline{uc}$ are compared with the values calculated from (3.12), both for the air and water flow experiments at $x=4h$ and $x=6h$ as seen in figure 25. The values of $\overline{uc}$ calculated from the model are in good agreement with the directly measured values. This is especially noteworthy considering that the model calculation is made up of the products of constant, at each x location, transport coefficients with the mean velocity and concentration gradients, $\partial\overline{U}/\partial y$ and $\partial\overline{C}/\partial y$, which are themselves measured values.

In table 2 the values of $\sqrt{D_1}$ are listed that gave the best fit of the model calculation to the measured data. When expressed as a fraction of the obstacle height, $\sqrt{D_1}/h$, the values are reasonably similar for the water and air flow experiments, but they become larger with distance downstream. As Wyngaard (1981) suggested, the turbulent transport coefficient, D_1, is of the order of the square of the large-eddy length scale, which, for this flow, should be of the order of the obstacle height, h.

That the model of $\overline{uc}$ in (3.12) agrees so well with the directly measured values implies that the models of $\overline{uv}$ and $\overline{vc}$ in (3.10) and (3.11) must represent these fluxes

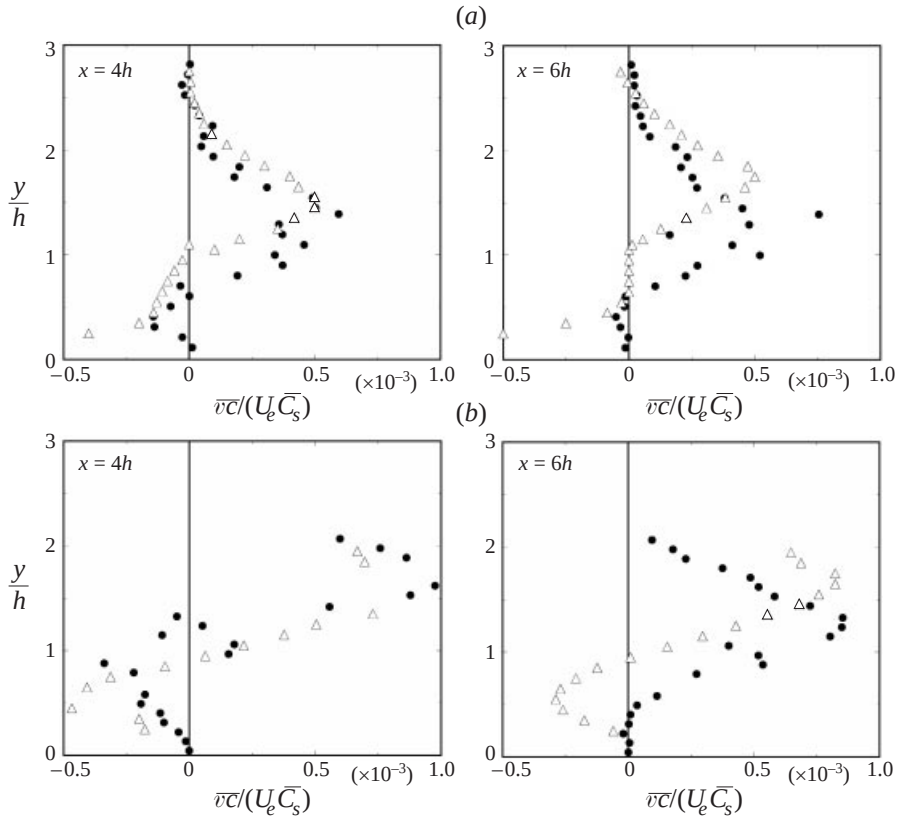

FIGURE 26. Vertical profiles of cross-stream scalar flux downstream of the obstacle. Comparisons between direct measurements and second-order gradient model equation (3.11). Filled circles, $\overline{vc}$ from measurements; open triangles from model. (*a*) Rhodamine B dispersion in water, $Sc \simeq 2500$ and (*b*) smoke dispersion in air, $Sc \simeq 10^6$. C_s is the source mean concentration and U_e is the external flow velocity.

	Water, $x = 4h$	Water, $x = 6h$	Air, $x = 4h$	Air, $x = 6h$
$\sqrt{D_1}$ (mm)	1.6	2.21	2.82	4.47
$\sqrt{D_1}/h$	0.22	0.32	0.28	0.45
K_v (cm^2 s^{-1})	0.098	0.14	3.22	6.42
$K_v/(U_e h)$	0.014	0.02	0.014	0.028
K_s (cm^2 s^{-1})	0.07	0.12	7.59	13.8
$K_s/(U_e h)$	0.01	0.017	0.033	0.06

TABLE 2. Scalar transport coefficients, $\sqrt{D_1}$ and K_s, and momentum transport coefficient, K_v, used in modelling the streamwise and cross-stream scalar fluxes, $\overline{uc}$ and $\overline{vc}$, and the momentum flux, $\overline{uv}$.

reasonably well at these two x/h positions in the flow where the wall-normal mean velocities are small.

Figure 26 shows the comparisons of the measured $\overline{vc}$ scalar flux values with those calculated with the model in (3.11). The eddy diffusivity coefficients, K_s, used in the calculation to obtain these best fits with the measured data also are listed in

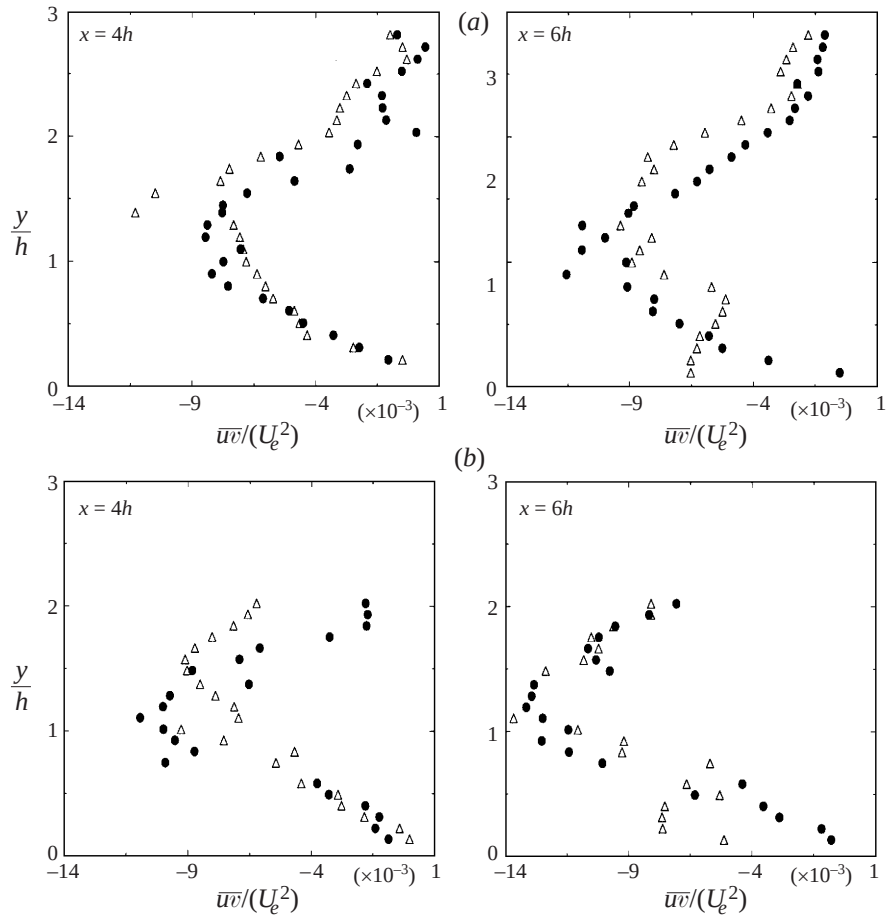

FIGURE 27. Vertical profiles of Reynolds stresses downstream of the obstacle. Comparisons between direct measurements and gradient model equation (3.10). Filled circles, $\overline{uv}$ from measurements; open triangles, from second-order model in (3.10). (*a*) In water, and (*b*) in air. U_e is the external flow velocity.

table 2. The agreement is reasonably good except at $x = 6h$. Both for the water and air flow experiments at this location, the position of the maximum $\overline{vc}$ values from the model approximation has shifted upward compared to the measured values. Nevertheless, the general shapes of the experimental profiles are reproduced by the model approximation, except near the wall for $y/h \leqslant 0.5$. When the values of the coefficient, K_s, are normalized with $U_e h$, they are of the same order of magnitude for the water and air experiment, but they nearly double with increased distance downstream from $x = 4h$ to $x = 6h$.

Figure 27 shows the comparisons of the measured $\overline{uv}$ momentum flux values with those calculated from the simple mean gradient model (3.10). Here the values of the eddy diffusivity coefficient, K_v, that gave the best match have been used and also are listed in table 2. The model is in good agreement with experimental data for both magnitude and shape except at $y \leqslant 0.5h$ at $x = 6h$. By comparing the K_s and K_v coefficients in table 2, it is seen that the streamwise scalar flux model (3.12) will be more sensitive to $\overline{vc}$ for the air flow than for the water flow.

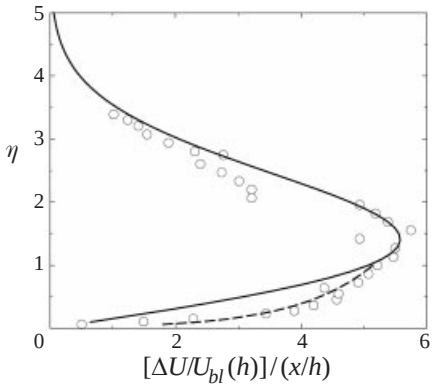

FIGURE 28. Mean velocity deficit profile in the wake region at $x = 20h$ compared to the similarity solution of Counihan *et al.* (1974): ○, measured values; ——, similarity solution in the mixing region; – – –, similarity solution near the wall.

3.6. *Similarity in the wake region*

The recirculation zone downstream of the obstacle extends to $x/h \approx 6.5$ in the present experiments. This is similar to the recirculation zone in the investigation by Counihan *et al.* (1974) that extended to approximately $6h$ for the flow downstream of a two-dimensional obstacle with $\delta/h = 8$. In order to make comparisons with and to extend the similarity analysis they carried out, we also made simultaneous measurements of the velocity and scalar concentration fields in the wake region for $x \geqslant 10h$, downstream of the recirculation region for the air flow. In figure 28 the mean streamwise velocity deficit profile at $x = 20h$ is compared with the similarity solution obtained by Counihan *et al.* (1974) and given by

$$\left.\begin{aligned} \frac{\Delta U}{\overline{U}_{bl}(h)}\left(\frac{x}{h}\right) &= \Delta U_{max}\, 2\eta\, \mathrm{e}^{-\eta^2/4} \\ \frac{\Delta U}{\overline{U}_{bl}(h)}\left(\frac{x}{h}\right) &= \Delta U_{max}\, 2\eta_o\, \mathrm{e}^{-\eta_o^2/4}\left[\frac{\ln\eta + \ln(\ell u_\tau/\nu)}{\ln\eta_o + \ln(\ell u_\tau/\nu)}\right]. \end{aligned}\right\} \tag{3.13}$$

The first expression in (3.13) is the solution for the mixing region of the wake, and the second is for the wall region, which extends up to about the level of the top of the obstacle. In these expressions $\eta = y/\ell$ is the cross-stream similarity position variable, $\eta_o \approx 1.05$ is the η position where the two expressions in (3.13) are matched, u_τ is the friction velocity of the obstacle-free flow and ℓ is the width of the mixing region, which is set equal to η_o. Additionally, ΔU is the deficit velocity as defined in § 3.1, i.e. the difference between the mean velocity at each x, y position with and without the obstacle in place, ΔU_{max} is the maximum value of the deficit for each x location profile with a value of -3.25 here at $x = 20h$, and $\overline{U}_{bl}(h)$ is the mean velocity of the obstacle-free boundary layer at the level h above the wall. Clearly the measured values agree quite well with the similarity solution in the two flow regions.

Encouraged by this good agreement for the velocity field, the similarity analysis of Counihan *et al.* (1974) was extended to the concentration field. The details of this analysis extension are given in Vinçont (1999), and it is outlined here. With the same assumptions made by Counihan *et al.* (1974) for the velocity field analysis, the

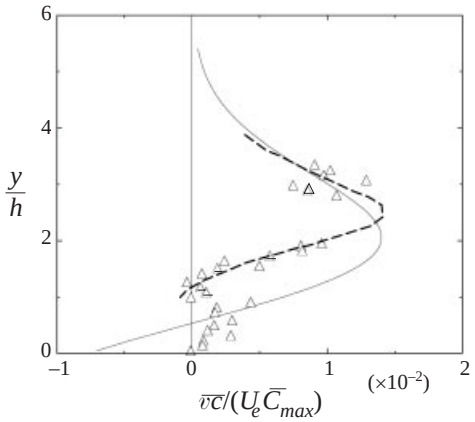

FIGURE 29. Cross-stream scalar flux profile in the wake region at $x = 20h$: △, measured values; – – –, smoothed measured values; ——, gradient model from (3.11). $\overline{C}_{max}$ is the maximum mean concentration value of the profile and U_e is external velocity.

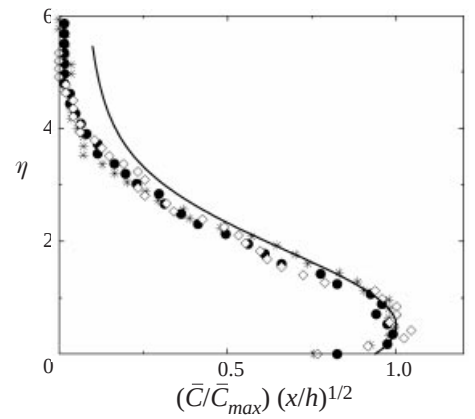

FIGURE 30. Self-similarity of mean concentration field in the wake at different positions downstream of the obstacle: filled circles, $x = 12h$; *, $x = 15h$; diamonds, $x = 20h$; ——, similarity solution from (3.15). The cross-stream similarity position is $\eta = y/\ell$, and ℓ is the width of the mixing zone.

evolution equation for the mean concentration reduces to

$$\overline{U}\,\frac{\partial \overline{C}}{\partial x} = -\frac{\partial \overline{vc}}{\partial y}, \tag{3.14}$$

where the undisturbed mean velocity, $\overline{U}$, was approximated by a constant value. The model expression for the cross-stream scalar flux in (3.11) can be used in (3.14), where, as for the recirculation region, the eddy-diffusivity coefficient, K_s, is taken to be constant and chosen so as to give the best fit to the measured $\overline{vc}$ profile, as shown in figure 29 for $x = 20h$. A function, $g(\eta)$, can then be sought such that

$$\overline{C} = \overline{C}_{max}(x/h)\,g(\eta), \tag{3.15}$$

where $\overline{C}_{max}$ is the maximum value of the mean concentration profile at the x location. From (3.11), (3.13), (3.14) and (3.15) the differential equation

$$2\,g''(\eta) + \eta\,g'(\eta) + g(\eta) = 0 \tag{3.16}$$

is obtained with the limiting conditions at $\eta = \frac{1}{2}$ such that $g(\frac{1}{2}) = 1$ and $(\mathrm{d}g/\mathrm{d}\eta)(\frac{1}{2}) = 0$, as can be seen in figure 30. The solution of (3.16) is

$$g(\eta) = \exp\left[-\tfrac{1}{4}\left(\eta^2 - \tfrac{1}{4}\right)\right]\left[1 - \tfrac{1}{2}\,\mathrm{dawson}(\tfrac{1}{4})\right] + \tfrac{1}{2}\,\mathrm{dawson}(\eta/2), \tag{3.17}$$

where the Dawson function is defined as

$$\mathrm{dawson}(\eta/\sqrt{2}) = -\tfrac{1}{2}\sqrt{\pi}\,\mathrm{i}\,\mathrm{e}^{-\eta^2/2}\,\mathrm{erf}(\mathrm{i}x/\sqrt{2}). \tag{3.18}$$

Of course, this solution is not valid at the wall, because $\overline{vc}$ must be zero there.

Figure 30 shows the comparison of our measured values of $\overline{C}/\overline{C}_{max}$ at $x = 12h$, $15h$ and $20h$ with the similarity expression in (3.15). The agreement up to $\eta = 3.5$ is quite good. Above this level (3.15) overestimates $\overline{C}$. At these higher η levels, the intermittency of the scalar field undoubtedly is a cause of this increasing lack of agreement. The solution is very good near the wall down to $\eta \approx 0.5$.

4. Conclusions

Simultaneous measurements of the velocity and scalar concentration fields in the plume emitting from a two-dimensional line source one obstacle height, h, downstream of a two-dimensional square obstacle placed on the wall of a turbulent boundary layer have been successfully carried out. These measurements were made with a combination of optical methods in both water and air. In addition to determining standard statistical properties of these fields at two locations in and above the recirculation region, a conditional analysis of the scalar fluxes was carried out, and, as a consequence, simple second-order mean gradient models for these fluxes were constructed and compared to the measurements. Finally, the similarity analysis of Counihan *et al.* (1974) for the velocity field in the wake region was compared to our measurements in this region at $x/h = 20$. This similarity analysis was then extended to the concentration field and compared to the mean concentration measurements at several x locations in the wake region. The principal results are the following.

(*a*) Preliminary tests without the obstacle on the wall of the boundary layer showed that the PIV measurements were sufficiently accurate in flow regions where the local mean shear is sufficiently small. For the complex flow downstream of the obstacle, this criterion was fulfilled reasonably well over much of the flow region.

(*b*) A stationary vortex with negative vorticity occurs just upstream of the obstacle, and a weaker stationary vortex with positive vorticity occurs just downstream. Scalar-laden fluid is pumped upward from the source slot between the latter vortex and the large recirculation zone where it is caught up in a reverse flow region just above and at the downstream end of the obstacle. The scalar is carried upstream, over the obstacle and then it is lifted further upward where it is convected downstream in the high-shear mixing region.

(*c*) At the downstream location $4h$ in the recirculation region, the mean streamwise velocity profile, $\overline{U}/U_e$, shows that reverse flow occurs below $y/h \approx 0.7$. This reverse flow region has almost disappeared at $6h$. The mean wall-normal velocity profile, $\overline{V}/U_e$, is slightly positive in this reverse flow region.

(*d*) In both water and air and at both $4h$ and $6h$, the normalized streamwise root-mean-square fluctuations, u'/U_e, are significantly larger than the normalized wall-normal fluctuations, v'/U_e. At both $4h$ and $6h$ the u'/U_e profiles have maxima above the level of the top of the obstacle. The v'/U_e profiles also have maxima in this region, but they are less pronounced.

(*e*) In both water and air the Reynolds shear stress profiles at $4h$ and $6h$ have

maxima just above the level of the top of the obstacle at about $1.1h$–$1.2h$ above the wall, i.e. in the mixing zone where the mean velocity gradient has its maximum. The Reynolds shear stress increases with downstream distance between $4h$ and $6h$.

(f) In both water and air the normalized mean scalar concentration, $\overline{C}/\overline{C}_s$, is largest, as expected, in the flow region immediately surrounding the source. Between $4h$ and $6h$ the mean concentration diminishes considerably in the recirculating zone. The root-mean-square values of the scalar concentration fluctuations are large in the mixing zone just above the level of the top of the obstacle. Between $4h$ and $6h$ $c'/\overline{C}_s$ diminishes as well, but not as much as the mean concentration.

(g) In both water and air, and at $4h$ and $6h$, the $\overline{uc}/U_e\overline{C}s$ profiles are positive in the recirculating zone, become negative at or just below the level of the top of the obstacle and have pronounced negative maxima at about $1.7h$ above the wall. These maxima diminish for both flows between $4h$ and $6h$.

(h) The $\overline{vc}/U_e\overline{C}_s$ profiles are negative in the recirculating zone approximately where the $\overline{uc}$ profiles are positive (except for the $4h$ profile in air). These profiles have their positive maxima somewhat higher than the $\overline{uc}/U_e\overline{C}_s$ profiles, i.e. between $1.2h$ and $1.8h$ above the wall.

(i) Conditional analysis of the data, by sorting them into the eight categories (octants) given by the sign combinations of the three variables, $\pm u$, $\pm v$ and $\pm c$, provided additional details about the scalar concentration transport processes in this complex flow. The octants with combinations of these three variables that correspond to types of scalar concentration flux motions that can be approximated by mean gradient scalar transport models are the octants that contribute most to $\overline{uc}$ and $\overline{vc}$ in all three zones of the flow downstream of the obstacle. However, in the recirculating zone, counter-gradient transport type motions also make significant contributions.

(j) Second-order mean gradient models of the scalar fluxes, $\overline{uc}$ and $\overline{vc}$, and the momentum flux, $\overline{uv}$, were constructed following the arguments of Wyngaard (1981). The agreement of the model calculation with the measured values of $\overline{uc}$ is excellent. The agreement with the measured values of $\overline{vc}$ is reasonably good at $x = 4h$, although it is not so good at $x = 6h$. However, qualitatively the model $\overline{vc}$ profile has the same shape as the experimental data profile at this location. The agreement of the model calculation with the experimental values of $\overline{uv}$ also is good except near the wall at the $6h$ stations.

(k) The measured profile of the mean deficit velocity at $x = 20h$ in the wake region was compared to the similarity profile of Counihan *et al.* (1974). The agreement is quite good. These similarity arguments were extended to the mean concentration field. Plotted in similarity variables, mean concentration profiles at $x = 12$, 15 and 20 collapse very well to a single self-similar profile. The computed profile from the similarity analysis agrees well with these measured profiles up to about $3h$ above the wall. For higher positions it is likely that the intermittency of the scalar plume is a cause of the increasing disagreement between the measured and calculated profiles.

The authors are grateful for the financial support of this research provided by the CNRS of France. Support of JMW while in France was provided by the Ministère de l'Enseignement Superieur et de la Recherche and DOE grant DE-FG02-94ER14441 as well as NSF grant INT-9726632. Vincent Chiang and Lawrence Ong generously provided parts of figure 7. We are grateful to Faouzi Laadhari for his LDA results concerning the water experiment and to Prof. J.-N. Gence for his help and comments on models.

Appendix. Post-processing of images

Here the processing of the concentration field and PIV field images, after they were recorded on analog video tape, will be discussed. The video tape images were digitized and treated in order to obtain the instantaneous velocity component and concentration information in the plane of the images. This information was then synchronized in time and space in order to obtain the scalar flux information sought in this plane.

A.1. *Digitization of images*

The PIV field CCD camera has 756×581 cells in the horizontal and vertical directions, respectively. However, odd and even lines of each video frame were used to record the successive images of each pair of images resulting from each pair of laser pulses. Thus the information was recorded in only 290 cells in the vertical direction on each video frame. These video frames were digitized by a 512×512 pixel 8 bit frame grabbing card of a PC, and the information stretching and compression that resulted from this process is linear. Thus the final resolution of the PIV digitized images was 512 pixels in the horizontal direction, but the information from the vertical 290 cells recorded on the analog video tape frames was linearly distributed to the 512 pixels in the vertical direction by the frame grabbing card. For the concentration field, even though the matrix of cells is slightly different, similar reasoning shows that the final resolution of the digitized images is the same as that for the PIV images. Thus the effective resolution of each image is 512 pixels horizontally and 290 pixels vertically. Each stored pixel had 256 grey levels.

A.2. *Treatment of PIV images*

Each of the PIV images was divided into small subzones with dimensions of 64×64 pixels. The treatment process determines the velocity components U and V, corresponding to the average movement of the particles in each subzone, by cross-correlating the successive subzone images for the time separation Δt of the laser pulses. Additional vectors can be obtained by overlapping the subzones as discussed in §§ 2.1 and 2.2; in this case the overlap was 50% in both the horizontal and vertical directions. This permits use of information about the displacement of the particles that are convected into and out of the subzones in the time Δt that otherwise would be lost. If there are insufficient numbers of particles in the subzone images, the velocity components in these subzones cannot be determined. An example of this problem is seen in the upper part of the instantaneous image in figure 8(*b*).

For these two experiments, the estimated average number of particles in each subzone, in the regions where the particles filled the flow, was about 20 for the water flow and 40 for the air flow. Only about half of these particles are common to the two successive images used in the cross-correlations, because the other half are convected in and out of the subzone fields of view. Thus an average of about 10 particles per subzone in water and 20 in air are common to the subzones in our flow cases. These common particles give the maxima in the cross-correlation calculations that correspond to the average particle displacements. Westerweel (1994) estimates that, with a minimum of four common particles per subzone, there is a 95% chance of obtaining a valid velocity vector. The method used here to determine automatically whether or not there was a sufficient number of particles in a given subzone was the following. For each subzone the average grey level of the instantaneous subzone image was determined and subtracted from the instantaneous grey level of each individual pixel of the subzone. The remainder pixel grey levels are the fluctuations about the

average. These were squared and added for the subzone pixel matrix to give the norm of the matrix. A threshold value was chosen between zero and large values of this pixel matrix norm by testing several examples. If, for a given instantaneous subzone, its pixel matrix norm value rose above the threshold value chosen, the algorithm indicated that a sufficient number of particles were present; if not, an insufficient number were present and no vector was calculated.

In the absence of a method to determine the cross-correlation peak location at a subpixel level, the average displacement of the particles in a subzone is taken to be the distance between the centre of the subzone and the centre of the pixel with the greatest correlation value. However, there are several methods to determine this peak location at the subpixel level. An overview is given by Lourenco & Krothapalli (1995). One of these methods assumes the correlation peak to be of some form, for example a Gaussian or a parabola, and the best fit of the experimental peak to this form is found by the least-squares method. One can improve the accuracy of this method by 'padding' the digitized fringe patterns with zeros (see Stearns & Hush (1990), and used by Simoëns (1992) and Simoëns & Ayrault (1994) for example), but this greatly increases the cross-correlation calculation time. An alternative method to improve accuracy is the two-dimensional reconstruction of Whittaker that provides the same accuracy as the Gaussian fit with zero padding, but is much faster. This is the subpixel method used in the present investigation. The method requires that the particle images contain a sufficient number of pixels to define well the form of the cross-correlation peak; this requirement is satisfied here. Using Whittaker's method (resulting from the Shannon theorie of subsampling) we were able to choose a subpixel accuracy of 0.2 pixels without much increase in the calculation time.

In order to obtain the proportional relationship between the physical dimensions in the flow and the recorded image and to check whether or not any distortion occurred, a Melles Griot target grid was placed in the illumination plane and its image recorded. With this information the particle displacements could be determined in terms of the physical dimension of the flow in the illumination plane.

A bandpass filter was used to eliminate large false velocity vectors. The band limits at each y level were chosen based on the PDFs of the measured U and V velocity components at that y level.

It is difficult to estimate the relative error of the PIV velocity component measurements. The absolute error due to limitations on the resolution of the positions of the particles for the streamwise component, U, is about 0.2 pixels. As explained above this is a consequence of our use of a subpixel method. The absolute error for the wall-normal velocity components, V, is twice that of U, i.e. 0.4 pixels. This difference is because the CCD camera that we used for PIV records separates even and odd lines as discussed above. These absolute pixel errors in determining particle positions give errors in the velocity components that are 4% and 8% in the x- and y-directions, respectively, relative to the peak r.m.s. values for both flows. Of course these relative errors increase as the r.m.s. values decrease downward toward the wall and upward above the shear layer.

A.3. *Treatment of concentration field images*

First, because the concentration and PIV field CCD cameras faced each other on each side of the illuminated plane, the concentration field images all needed to be reversed in order to give them the same orientation as those of the PIV field. This was systematically carried out.

Second, as mentioned in § 2.1, the background light for both the water and air flows,

with the pair of aperture openings of each flow corresponding to the downstream and source light intensities respectively, was recorded with no scalar released and without the lasers pulsing. These background images were digitized and averaged. The grey levels of each pixel of these average background images for each of the two aperture openings corresponding to the two flows were then subtracted from the corresponding pixel grey levels of each image for each of the corresponding flow and aperture opening conditions. As a result of this subtraction process, all the images had their background light removed. At this point the optical property of the lenses that gives precisely a factor of 2 in light intensity between two successive aperture openings could be utilized. For the water flow there are four aperture steps, and for the air flow there are five steps between the source and downstream recorded images. Thus, the light intensity of the source images could be multiplied by 2^4 and 2^5 for the water and air flows, respectively, in order to obtain the equivalent light intensity at the source corresponding to the aperture openings used to record the images of the plume downstream. The light intensity of the downstream images could subsequently be divided by these treated source images to obtain the relative light intensity. This relative light intensity is linearly proportional to the relative scalar concentration of the fluorescent dye in the water flow under the conditions discussed in § 2.1. It is also linearly proportional to the relative scalar concentration of the 'equivalent' monodispersed smoke particles in the air flow as discussed in § 2.2.

A.4. *Treatment of concentration fluxes*

With the image treatments described above, instantaneous values of the U and V velocity components and of the scalar concentration, temporally synchronized, were stored and available to calculate the concentration fluxes. Before this could be done, however, the velocity and concentration information had to be spatially compatible. Before the flow images were recorded, a spatial grid, drawn on a transparency, was placed in the illumination plane with its bottom side on the wall. This grid was imaged by both cameras and, after these images were digitized, they provided precise positioning and dimensions of the common field of view of the two CCD cameras. With this information it was possible to know exactly what subzones in the concentration field images corresponded to the subzones of the PIV images. The 64×64 pixels of the PIV subzones for both the water and air flow images correspond to 12×12 pixels of the concentration subzones for the water flow and 5×5 pixels for the air flow. It was necessary to choose the number of pixels, about the centres of these concentration subzones, that would be averaged to obtain the concentration values to correlate with the corresponding velocity values in order to obtain instantaneous concentration flux values. The useful particles of each PIV subzone that were involved in the calculation of its correlation peak were estimated to be in the middle quarter. Thus the spatial resolution of the velocity component measurements is considerably better than the size of the subzones. Furthermore, the scales of the concentration fluctuations are considerably smaller than those of the velocity fluctuations. Thus, the concentration values used for all the calculations were obtain from the central four pixels forming a square about the centre of the concentration subzone (see Papanicolaou & List 1988). It was decided not to use a single pixel in order to preclude the errors caused by any single pixel having a seriously incorrect grey level. An empirical test was carried out to determine how much the statistics change with the number of pixels over which the spatial average concentrations are determined. For 1 or 2×2 pixels, the change was insignificant, but the r.m.s. values of c were significantly reduced when a greater number of pixels was used.

At this stage in the treatment of the images, the instantaneous velocity components and relative scalar concentration values were synchronized in time and had a compatible resolution at each spatial location of the subzones. With these values the mean and root-mean-square velocity component and concentration values could be calculated as well as the concentration flux values. 1000 image pairs for each position of the PIV CCD camera were so treated to obtain these statistics. Tests were done to determine the minimum number of images necessary to obtain converged velocity and concentration fluctuation moments of different orders. It was found that second and third moments converged reasonably well with 1000 images, but fourth moments showed scatter due to lack of convergence.

In the air flow case the same incense particles were used to determine the velocity field components and the relative scalar concentration. To understand an additional difficulty in obtaining unconditioned scalar flux values, consider the following identity:

$$\overline{u_i c} = \overline{U_i C} - \overline{U_i}\ \overline{C}. \tag{A 1}$$

The left-hand side of the equation is the unconditional scalar flux, $\overline{u_i c}$, to be measured. The first term on the right-hand side is the average of the product of the instantaneous velocity component value, U_i, and the instantaneous concentration value, C. The second term on the right-hand side is the product of the mean values, $\overline{U_i}$ and $\overline{C}$. The instantaneous U_i values cannot be determined if insufficient particles are present in a subzone, for example near the boundary of the smoke plume such as in the images in figure 8(*b*). If this is the case, however, the instantaneous C values in the subzones are nearly zero, so their products with the unknown values of U_i are also, necessarily, nearly zero. Thus the average flux values, $\overline{U_i C}$, are correct, even though the U_i values in the averages cannot be determined for the instances when insufficient particles are present. All that remains to be determined are the individual mean values, $\overline{U_i}$ and $\overline{C}$. The values of $\overline{C}$ are correctly determined from the plume images. However, if the PIV images obtained from the smoke plume are used to measure $\overline{U_i}$, these mean values will be conditioned by the intermittency of the smoke in the subzones of the plume boundary regions. Thus an independent, unconditional measurement of $\overline{U_i}$ was made by separately seeding the entire boundary layer with smoke and obtaining PIV images of this flow without a smoke plume.

REFERENCES

Antonia, R. A., Prahu, A. & Stephenson, S. E. 1975 Conditionally sampled measurements in a heated turbulent jet. *J. Fluid Mech.* **72**, 455–480.

Ayrault, M. & Simoëns, S. 1995 Turbulent concentration determination in gas flow using multiple CCD cameras. *J. Flow Visualization Image Processing* **2**, 195–208.

Britter, R. E. 1989 Experiments on some effects of obstacles on dense-gas dispersion. *AEA Rep. SRD* R 407.

Browne, L. W. B. & Antonia, R. A. 1986 Reynolds shear stress and heat flux measurements in a cylinder wake. *Phys. Fluids* **29**, 709–713.

Counihan, J., Hunt, J. C. R. & Jackson, P. S. 1974 Wakes behind two-dimensional surface obstacles in turbulent boundary layers. *J. Fluid Mech.* **64**, 529–563.

Dinar, N., Kaplan, H. & Kleinmann, M. 1988 Characterization of concentration fluctuations of a surface plume in a neutral boundary layer. *Boundary Layer Met.* **45**, 157–175.

Fackrell, J. E. & Robins, A. G. 1982 Concentration fluctuations and fluxes in plumes from point sources in a turbulent boundary layer. *J. Fluid Mech.* **117**, 1–26.

Gad-el-Hak, M. & Morton, J. B. 1979 Experiments on the diffusion of smoke in isotropic turbulent flow. *AIAA J.* **177**, 558–562.

GONG, W. 1991 A wind tunnel study of turbulent dispersion over two- and three-dimensional gentle hills from upwind point sources in neutral flow. *Boundary Layer Met.* **54**, 211–230.

LEMOINE, F., WOLFF, M. & LEBOUCHE, M. 1996 Simultaneous concentration and velocity measurements using combined laser-induced fluorescence and laser Doppler velocimetry: Application to turbulent transport. *Exps. Fluids* **20**, 319–327.

LOURENCO, L. & KROTHAPALLI, A. 1995 On the accuracy of velocity and vorticity measurements with PIV. *Exps. Fluids* **18**, 421–428.

MOENG, C.-H. & WYNGAARD, J. C. 1989 Evaluation of turbulent transport and dissipation closures in second-order modeling. *J. Atmos. Sci.* **46**, 2311–2330.

PAPANICOLAOU, P. N. & LIST, E. J. 1988 Investigations of round vertical turbulent buoyant jets. *J. Fluid Mech.* **195**, 341–391.

PAPANTONIOU, D. & LIST, E. J. 1989 Large scale structure in the far field of buoyant jets. *J. Fluid Mech.* **209**, 151–190.

POREH, M. & CERMAK, J. E. 1964 Study of diffusion from a line source in a turbulent boundary layer. *Intl J. Heat Mass Transfer* **7**, 1083–1095.

ROTTA, J. C. 1951 Statistische theorie nicht-homogener turbulenz. *Zeit. Phys.* **129**, 547–572.

SAWFORD, B. L., FROST, B. L. & ALLAN, T. C. 1985 Atmospheric boundary-layer measurements of concentration from isolated and multiple sources. *Boundary Layer Met.* **31**, 249–268.

SCHOFIELD, W. H. & LOGAN, E. 1990 Turbulent shear flow over surface mounted obstacles. *Trans. ASME:* I: *J. Fluids Engng* **112**, 376–385.

SIMOËNS, S. 1992 Application du traitement et de l'analyse d'images a des phénoménes de dispersion et de mélange turbulents. Thése de Doctorat de l'Ecole Centrale de Lyon.

SIMOËNS, S. & AYRAULT, M. 1994 Concentration flux measurements of a scalar quantity in turbulent flows. *Exps. Fluids*, **16**, 273–281.

SIMOËNS, S., AYRAULT, M., PRIMON, R. & VERDUZIO, G. 1996 Simultaneous velocity and concentration measurements using Mie scattering and particle image velocimetry in a turbulent air jet. *Intl Seminar on Optical Methods and Data Processing In Heat and Fluid Flow: IMechE Conf. Trans. 1996-3*, Part C., pp. 301–308. MEP Publications, London.

SPALART, P. 1988 Direct simulation of a turbulent boundary layer up to $Re_\theta = 1410$. *J. Fluid Mech.* **187**, 61–98.

SPALDING, D. 1961 A single formula for the law of the wall. *Trans. ASME* C: *J. Appl. Mech.* **28**, 455–458.

STEARNS, S. D. & HUSH, D. 1990 *Digital Signal Analysis*, 2nd Edn, pp. 75–84, Prentice Hall.

TROMBETTI, F. & TAMPIERI, F. 1992 Analysis of wind tunnel dispersion data over two-dimensional obstacles. *Boundary Layer Met.* **59**, 209–226.

VINÇONT, J.-Y. 1999 Détermination des flux turbulents de masse dans le sillage d'un obstacle: Application à l'écoulement à l'intérieur de la canopée urbaine. These de Doctorat de l'Ecole Centrale de Lyon.

WALLACE, J. M., BERNARD, P. S., CHIANG, K. S. & ONG, L. 1995 Contaminant dispersal in bounded turbulent shear flow. *Proc. Thirteenth Symp. on Energy Engng Sci.*, Argonne National Lab. Conf., pp. 177–185.

WALLACE, J. M., ECKELMANN, H. & BRODKEY, R. S. 1972 The wall region in turbulent shear flow. *J. Fluid Mech.* **54**, 39–48.

WESTERWEEL, J. 1994 Efficient detection of spurious vectors in particle image velocimetry data. *Exps. Fluids* **16**, 236–247.

WYNGAARD, J. C. 1981 *Atmospheric Turbulence and Air Pollution Modelling* (ed. F. T. M. Niewstadt & H. Van Dop), pp. 69–106. D. Reidel.